

Study of instability of the Fourier split-step method for the massive Gross–Neveu model

T.I. Lakoba*

Department of Mathematics and Statistics,
University of Vermont, Burlington, VT 05405, USA

November 5, 2019

Abstract

Stability properties of the well-known Fourier split-step method used to simulate a soliton and similar solutions of the nonlinear Dirac equations, known as the Gross–Neveu model, are studied numerically and analytically. Three distinct types of numerical instability that can occur in this case, are revealed and explained. While one of these types can be viewed as being related to the numerical instability occurring in simulations of the nonlinear Schrödinger equation, the other two types have not been studied or identified before, to the best of our knowledge. These two types of instability are *unconditional*, i.e. occur for arbitrarily small values of the time step. They also persist in the continuum limit, i.e. for arbitrarily fine spatial discretization. Moreover, one of them persists in the limit of an infinitely large computational domain. It is further demonstrated that similar instabilities also occur for other numerical methods applied to the Gross–Neveu soliton, as well as to certain solitons of another relativistic field theory model, the massive Thirring.

Keywords: Fourier split-step method; numerical instability; solitary waves; massive Gross–Neveu model; nonlinear Dirac equations.

*tlakoba@uvm.edu, 1 (802) 656-2610

1 Introduction

The split-step, or operator-splitting, method (SSM) is one of the most widely used numerical tools to model evolution of linear and nonlinear waves. It is explicit (hence straightforward to code), has a number of desirable structure-preserving properties (e.g., preserves the L_2 -norm exactly in Hamiltonian systems and is symplectic), is easy to implement with the 2nd-order accuracy in time [1], and allows algorithmic extensions for higher-order accurate implementations [2, 3, 4, 5]. The idea of the SSM for wave equations is to account for linear terms with spatial derivatives, on one hand, and for all other terms, on the other hand, in separate substeps, where each of these substeps can be performed more efficiently than a step corresponding to the full evolution. A popular method to implement the substep accounting for linear terms with spatial derivatives is via (fast) discrete Fourier transform and its inverse; hence the name ‘Fourier’ (or ‘spectral’) in the corresponding version of the SSM. A vast body of literature exists on just the Fourier version of the SSM, not to mention its other (e.g., finite-difference) versions. In what follows *we will consider only the Fourier SSM and therefore will omit the modifier ‘Fourier’* unless a different version of the SSM will be referred to. A (far from complete) list of application of this numerical method, focusing *only on nonlinear Hamiltonian* systems, includes: the nonlinear Schrödinger equation (NLS) [6, 7]

$$iu_t + u_{xx} + |u|^2u = 0; \tag{1}$$

Gross–Pitaevskii equation (i.e., NLS with a potential term) with a magnetic field term [8]; Vlasov–Poisson equations [9]; nonlinear Dirac equations in one spatial dimension [10]

$$\begin{aligned} \psi_{1,t} + \psi_{2,x} &= i(|\psi_1|^2 - |\psi_2|^2 - 1)\psi_1, \\ \psi_{2,t} + \psi_{1,x} &= -i(|\psi_1|^2 - |\psi_2|^2 - 1)\psi_2; \end{aligned} \tag{2}$$

generalized Zakharov equations [11, 12]; and Korteweg–de Vries equation [6].

Since the SSM is an explicit method, it can be only conditionally stable. Its numerical (in)stability was extensively studied for the NLS in one spatial dimension. In [13], the von Neumann analysis was applied to the SSM simulating a solution close to the plane wave, and the (in)stability threshold and the instability growth rates were found. Specifically, the instability threshold in this case is:

$$\Delta t_{\text{thresh}} = \Delta x^2 / \pi, \tag{3}$$

where Δt and Δx are discretization steps in time and space. The quadratic dependence in (3) is a consequence of the “resonance”, or “phase matching”, condition

$$\omega \Delta t = \pi n, \quad n \in \mathbb{N}, \tag{4a}$$

and the dispersion relation of the linear part of the NLS:

$$\omega = k^2, \tag{4b}$$

where ω is the frequency and $k \in [-k_{\text{max}}, k_{\text{max}})$ is the wavenumber;

$$k_{\text{max}} = \pi / \Delta x. \tag{4c}$$

Long-term behavior of the solution obtained by the SSM for the NLS with small and localized initial data was studied in [14] by the modulated Fourier expansion and in [15] by the Birkhoff normal form analysis. In [16], stability of the near-soliton (i.e., localized, not small-norm) solution was considered by a modified equation technique. While the instability threshold for the near-soliton solution is still given by (3), the instability growth rate was found to be significantly smaller than that for the plane-wave case.

Given the wide popularity of the SSM for NLS-type models, it is not surprising that it was also used extensively in studying solutions of the Gross–Neveu model (2). In numerical simulations of [17, 18, 19], SSM’s performance for this model was favorably compared to that of other methods. In recent studies [20, 21], it was shown that the SSM is capable of resolving distinctly different scales, i.e., of efficiently obtaining highly-oscillatory solutions, that occur in the non-relativistic regime of (2). This method was also studied in [22] for the massive Thirring model, which is closely related to (2). In Section 7 we will show that there are close similarities not only in the analytical, but also in the numerical, solution of the two models. The equations of Bragg solitons in nonlinear fiber optics, which are an extension of the Thirring model and thus are also mathematically related to the Gross–Neveu model, have been also often simulated by the SSM (see, e.g., [23, 24, 25, 26]). It is relevant to note that this method is also widely used in simulations of linear Dirac–Maxwell systems; see the original paper [27] and a recent study [28].

Despite this significant activity, stability of the SSM for the Gross–Neveu (or any other nonlinear spinor) model was studied analytically only in [10]. However, the instability threshold obtained therein appears to contradict both our analysis and numerical evidence, presented in Sections 4 and 3.1, respectively. On the other hand, in [17, 18, 19] it was stated without a proof that the SSM is unconditionally stable for the Gross–Neveu model. While this may be correct for some small-norm solutions, it is *not* correct for essentially nonlinear solutions, such as the soliton.

In this work, we show analytically and verify by extensive numerical simulations that the 2nd-order SSM applied to the soliton of nonlinear spinor models, including the Gross–Neveu model (2), can exhibit *unconditional* numerical instability (NI) via two distinctly different mechanisms. Not only does this NI persist as $\Delta t \rightarrow 0$, but it is also *not* suppressed by taking $\Delta x \rightarrow 0$. Thus, no matter how fine a discretization in both space and time one uses, the numerical solution of (2) by the SSM will eventually become invalid. Moreover, for one of the two mechanisms, the NI is also not suppressed by taking an increasingly large computational window. For a certain range of the soliton parameters, this NI is strong enough to destroy the solution even over moderately (as opposed to very) long times. We will also show that this NI can occur for other nonlinear spinor models, as well as for other numerical methods applied to such models.

It should be noted that numerical instabilities of the Gross–Neveu soliton have previously been reported [29, 30] by methods other than the SSM. The main differences between our work and those studies are in that: (i) we reveal the mechanisms (i.e., the forms of coupling between different Fourier modes) via which NI can occur, and (ii) we *systematically* study the dependence

of NI’s characteristics on the computational parameters, such as Δt , Δx , and the computational domain length L . Further differences will be discussed in Section 8.

Our analysis of the unconditional NI mechanisms for the Gross–Neveu solitons will be semi-numerical. That is, while we will be able to identify *how* coupling among different Fourier modes can drive them towards NI, the corresponding equations will turn out to be too complicated to allow analytical treatment and therefore have to be solved numerically. We believe that this is still valuable for at least two reasons other than the conceptual reason of understanding NI mechanisms, which can also appear in other models and numerical methods. First, our analysis allows us to obtain the dependence of the most important NI parameter — its growth rate — on the parameters of the simulated solution and of the numerical scheme in a matter of seconds or at most minutes, whereas direct numerical simulations by the SSM may take hours (when one considers limits such as $\Delta t \rightarrow 0$, $\Delta x \rightarrow 0$, or $L \rightarrow \infty$). Second, knowing for what Fourier modes the NI arises, and how its growth rate depends on the problem parameters, may help one to tell a NI from a true physical instability. The latter does not occur for the soliton of (2) [31], but does occur in models with nonlinearity higher than cubic (see, e.g., [29, 30]).

The main part of this paper is organized as follows. In Section 2 we will summarize relevant facts about the soliton solution of the Gross–Neveu model. In Section 3 we will present simulation results which illustrate manifestations of NI and thus will provide motivation for the analyses in later sections. We will begin, in Section 4, by analyzing the possibility of a *conditional* NI, not mentioned above. For that, we will derive a counterpart of an instability threshold (3) for the Gross–Neveu model. However, unlike the NLS case, here we will show that even when the time step exceeds such a “threshold”, *high-k* Fourier modes near the corresponding “resonant” value k_π will *not* grow exponentially unless the soliton is subject to a *low-k* instability (whether physical or numerical).

In Section 5, we will analyze the unconditional NI that occurs near the edges of the computational spectral window. In Section 6 we will analyze a different kind of unconditional NI, whereby *all modes* sufficiently remote from the spectral window’s edges and from $k \approx 0$ become exponentially unstable. In order to carry out the analyses in these two sections, we have to assume that the background solution is a single soliton, perturbed infinitesimally. In Section 7 we will demonstrate that the unconditional NIs occur in a significantly wider variety of applications than the specific problem analyzed in those sections. Namely, we will show that these NIs can be observed when the background solution is of a more general form than a single soliton, when the SSM is applied to models similar to, but other than, the Gross–Neveu, and that they are also observed in other popular numerical methods applied to such models. We also briefly discuss how such NIs can be suppressed. In Section 8 we present conclusions of this study and discuss the relation of its findings with those of [29, 30]. *The reader who is not interested in technical details, may read only Sections 2, 3, and 8.*

Since our numerical results pertaining to unconditional NIs of the SSM may appear counter-

intuitive to the reader, in Appendix A we present a short Matlab code that can be used to reproduce all of the reported results for the SSM and the Gross–Neveu soliton. In Appendix B we discuss in some detail the issue of “fragility” of the Gross–Neveu soliton, introduced in Section 2. Appendices C and D contain technical results related to the analysis in Sections 5 and 6, respectively.

2 Soliton solution of the Gross–Neveu model and its stability

The standing soliton solution of the Gross–Neveu model (2) is [33]:

$$\psi_1 = \Psi_1(x) e^{-i\Omega t}, \quad \psi_2 = \Psi_2(x) e^{-i\Omega t}, \quad \Omega \in (0, 1); \quad (5a)$$

$$\Psi_1(x) = \frac{\sqrt{2(1-\Omega)} \cosh(\beta x)}{\cosh^2(\beta x) - \mu^2 \sinh^2(\beta x)}; \quad \Psi_2(x) = i\mu \tanh(\beta x) \Psi_1(x); \quad (5b)$$

with $\beta = \sqrt{1-\Omega^2}$ and $\mu = \sqrt{(1-\Omega)/(1+\Omega)}$. Representative members of this family for different values of Ω are shown in Fig. 1.

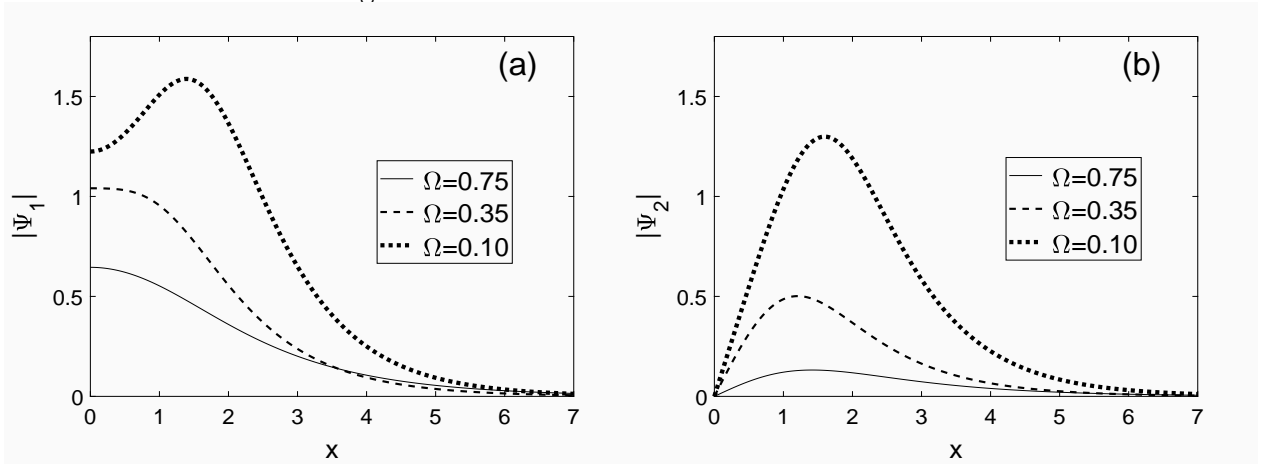


Figure 1: Components Ψ_1 (a) and Ψ_2 (b) of soliton (5). By symmetry, $\Psi_1(-x) = \Psi_1(x)$ and $\Psi_2(-x) = -\Psi_2(x)$.

A soliton moving with velocity $V \in (-1, 1)$ is obtained from (5) by a Lorentz transformation (see, e.g., [34]):

$$\begin{pmatrix} \Psi_{1,\text{mov}}(x, t) \\ \Psi_{2,\text{mov}}(x, t) \end{pmatrix} = \frac{1}{\sqrt{2}} \begin{pmatrix} \sqrt{\Gamma+1} & \sqrt{\Gamma-1} \\ \sqrt{\Gamma-1} & \sqrt{\Gamma+1} \end{pmatrix} \begin{pmatrix} \Psi_1(x_{\text{mov}}, t_{\text{mov}}) \\ \Psi_2(x_{\text{mov}}, t_{\text{mov}}) \end{pmatrix}, \quad (6a)$$

where

$$\Gamma = 1/\sqrt{1-V^2}, \quad x_{\text{mov}} = \Gamma(x - x_0 - Vt), \quad t_{\text{mov}} = \Gamma(t - V(x - x_0)). \quad (6b)$$

For future reference we present the Gross–Neveu equations linearized on the background of the soliton (5). They are obtained by substitution of

$$\psi_{1,2} = \left(\Psi_{1,2}(x) + \tilde{\psi}_{1,2}(x, t) \right) e^{-i\Omega t}, \quad \left| \tilde{\psi}_{1,2} \right| \ll 1 \quad (7)$$

into Eqs. (2) and discarding terms nonlinear in $\tilde{\psi}_{1,2}$. Defining a vector $\tilde{\boldsymbol{\psi}} = (\tilde{\psi}_1, \tilde{\psi}_2)^T$, one can write the linearized Eqs. (4) in the form:

$$\tilde{\boldsymbol{\psi}}_t - i\Omega \tilde{\boldsymbol{\psi}} + \boldsymbol{\sigma}_1 \tilde{\boldsymbol{\psi}}_x = i\mathbf{P}(x)\tilde{\boldsymbol{\psi}} + i\mathbf{Q}(x)\tilde{\boldsymbol{\psi}}^* \quad (8a)$$

where Pauli matrices are:

$$\boldsymbol{\sigma}_0 = \begin{pmatrix} 1 & 0 \\ 0 & 1 \end{pmatrix}, \quad \boldsymbol{\sigma}_1 = \begin{pmatrix} 0 & 1 \\ 1 & 0 \end{pmatrix}, \quad \boldsymbol{\sigma}_2 = \begin{pmatrix} 0 & -i \\ i & 0 \end{pmatrix}, \quad \boldsymbol{\sigma}_3 = \begin{pmatrix} 1 & 0 \\ 0 & -1 \end{pmatrix}, \quad (8b)$$

and $\mathbf{P} \equiv \sum_{j=0}^3 \boldsymbol{\sigma}_j P_j$, $\mathbf{Q} \equiv \sum_{j=0}^3 \boldsymbol{\sigma}_j Q_j$ with:

$$P_0 = \frac{1}{2} (|\Psi_1|^2 + |\Psi_2|^2), \quad P_1 = 0, \quad P_2 = \text{Im}(\Psi_1 \Psi_2^*), \quad P_3 = \frac{3}{2} (|\Psi_1|^2 - |\Psi_2|^2) - 1; \quad (8c)$$

$$Q_0 = \frac{1}{2} (\Psi_1^2 + \Psi_2^2), \quad Q_1 = -\Psi_1 \Psi_2, \quad Q_2 = 0, \quad Q_3 = \frac{1}{2} (\Psi_1^2 - \Psi_2^2). \quad (8d)$$

In (8c) we have used the fact that $\text{Re}(\Psi_1^* \Psi_2) = 0$. Equation (8a) can be rewritten in another form which will be convenient to refer to in what follows:

$$\left(\begin{array}{c} \tilde{\boldsymbol{\psi}} \\ \tilde{\boldsymbol{\psi}}^* \end{array} \right)_t = \mathcal{L} \left(\begin{array}{c} \tilde{\boldsymbol{\psi}} \\ \tilde{\boldsymbol{\psi}}^* \end{array} \right), \quad \mathcal{L} = \begin{pmatrix} i\boldsymbol{\sigma}_0\Omega - \boldsymbol{\sigma}_1\partial_x & 0 \\ 0 & -i\boldsymbol{\sigma}_0\Omega - \boldsymbol{\sigma}_1\partial_x \end{pmatrix} + \begin{pmatrix} i\mathbf{P}(x) & i\mathbf{Q}(x) \\ -i\mathbf{Q}^*(x) & -i\mathbf{P}^*(x) \end{pmatrix}. \quad (9)$$

Let us note that in Eqs. (8) and (9) and everywhere below, a lower-case and upper-case boldface letters indicate (2×1) vectors and (2×2) matrices, respectively.

An important issue for the study of the stability of the numerical method, which we will undertake in subsequent sections, is the *physical* (as opposed to numerical) stability of the soliton (5). By this we mean stability of the soliton of the original partial differential equation (2) (i.e., regardless of any numerical scheme) to small perturbations of its initial profile. This is often referred to as linear, or spectral, stability. To that end, we note that, on one hand, the soliton was semi-analytically proved to be spectrally stable [31]. On the other hand, numerical simulations by various methods detected a slow instability of an unknown origin [29] for $\Omega \lesssim 0.56$ in (5). In [32] we numerically demonstrated, by a non-Fourier SSM, that the Gross–Neveu soliton is linearly stable, as predicted semi-analytically in [31], for $\Omega \geq 0.01$ (and we had no evidence to suspect that it could be unstable for smaller Ω). However, we also confirmed the observation of [29, 30] that for sufficiently small Ω the soliton gets increasingly (as Ω decreases) “fragile” with respect to small perturbations. According to numerical evidence, such a perturbation may be either due to a permanently active driving source, such as the discretization error of the numerical scheme, or due to the initial condition not being the exact soliton. (In the latter case, the soliton “sheds” the excess field into dispersive radiation, which affects the soliton by passing through it.) The origin of this empirically observed fragility is not presently understood. In Appendix B we present cursory evidence that it is related to some instability of certain low- k Fourier harmonics, which may occur due to the finite size of the computational domain. In this work we do not further discuss this issue. However, two clarifications are in order.

First, we will refer to solitons that exhibit such a fragile behavior as *fragile*, as opposed to unstable. The latter term may trigger a confusion with linear instability, which would be incorrect, given that the soliton is linearly stable (see above). The term ‘fragile’ is, admittedly, not conventional in the mathematical literature, but it does accurately describe the empirically observed soliton’s behavior. Namely, a fragile soliton may be destroyed relatively quickly by the presence of a perturbation that is several orders of magnitude smaller than the soliton.

Second, it should be noted that the value $\Omega \approx 0.56$ reported in [29] is not to be regarded as a sharp threshold between fragile and non-fragile behaviors. In Appendix B we present numerical evidence that weakly fragile behavior occurs for the soliton with $\Omega = 0.75$. We believe that there is no sharp boundary between non-fragile and fragile behaviors, and whether one observes signs of the latter depends on Ω , L , and the computational time. We therefore arbitrarily set $\Omega = 0.6$ as a mark separating the two types of behavior. For $\Omega = 0.6$, one does not observe distinct signs of fragile behavior for $L \gtrsim 100$ and $t \lesssim 10,000$, and thus we refer to the corresponding solitons as non-fragile. Solitons with $\Omega < 0.6$ will then be referred to as fragile.

3 Numerical examples motivating subsequent analysis

In the three subsections of this section we will provide results of numerical simulations that demonstrate three different types of behavior of the SSM applied to the Gross–Neveu soliton (5) which have not been observed for the NLS soliton.

In all simulations reported below we used the 2nd-order SSM, for which the evolution over one time step has the form:

$$\begin{pmatrix} \psi_1 \\ \psi_2 \end{pmatrix} (x, t + \Delta t) = \exp [i(\Delta t/2)\mathcal{D}] \exp [i\Delta t\mathcal{N}] \exp [i(\Delta t/2)\mathcal{D}] \begin{pmatrix} \psi_1 \\ \psi_2 \end{pmatrix} (x, t), \quad (10)$$

where \mathcal{D} is the spatial-derivative operator on the left-hand side (l.h.s.) of (2) and \mathcal{N} is the operator on the r.h.s. of that system. As stated in the Introduction, here \mathcal{D} is implemented via discrete Fourier transform (15). The initial condition is taken as the soliton plus a white noise of size $\sim 10^{-12}$ in the x -domain.

3.1 Linear numerical instability is *not* inevitable for $\Delta t > “\Delta t_{\text{thresh}}”$

To put the forthcoming results in context, we note that the same logic that led one from Eqs. (4) to (3), along with the asymptotically (for large k) linear dispersion relation

$$\omega = \pm k \quad (11)$$

of (2), suggests that the NI threshold for the Gross–Neveu model should be

$$\Delta t_{\text{thresh}} = \Delta x. \quad (12)$$

Below we will show that this is *not* always the case.

In Fig. 2 we report simulation results for a non-fragile soliton with $\Omega = 0.75$ (see Fig. 1). Other parameters are: domain length $L = 20\pi$; number of grid points $N = 2^{16}$, so that $\Delta x \approx 9.6 \cdot 10^{-4}$; and simulation time $t_{\max} = 10,000$. (An explanation for using such a small Δx is found in the next paragraph.) Figure 2(a) shows that when $\Delta t < \Delta x$, no sign of NI is observed. When we increase Δt to fall in the interval $(n\Delta t_{\text{thresh}}, (n+1)\Delta t_{\text{thresh}})$, where Δt_{thresh} is defined by (12) and $n \in \mathbb{N}$, we observe (see Figs. 2(b)–(d)) $2n$ spectral peaks around wavenumbers $\pm k_{\pi}, \dots, \pm k_{n\pi}$, where

$$k_{n\pi} = n\pi/\Delta t; \quad (13)$$

see Section 4 for a derivation. However, these peaks grow *not* exponentially in time, but only linearly. We verified this fact for several different sets of $(\Omega, L, \Delta x, \Delta t)$. We were unable to explain the origin of these peaks and therefore will not discuss them below. However, we emphasize that due to their linear, as opposed to exponential, growth, they do not present a real problem for any but extremely long-time (on the order of many million time units) simulations.

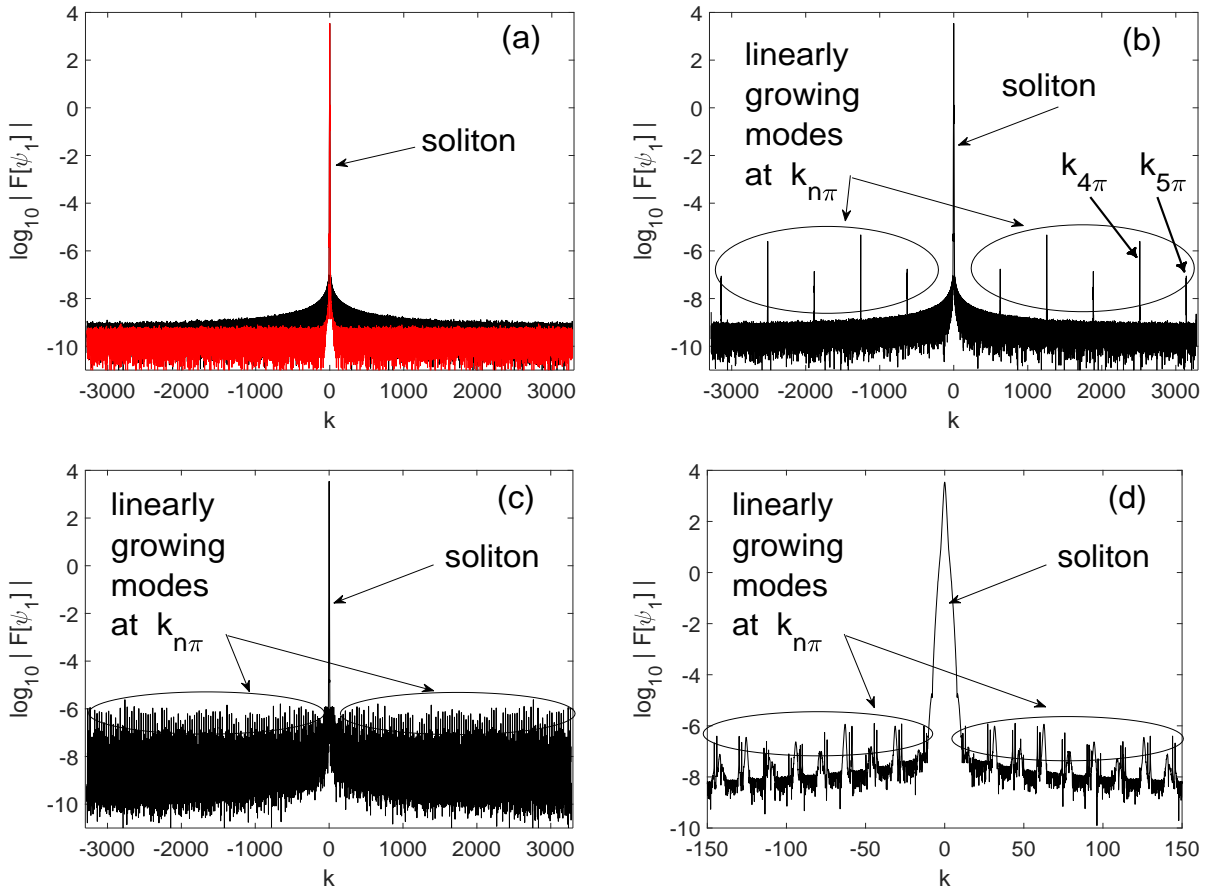


Figure 2: Numerical solution's spectrum for the initial soliton with $\Omega = 0.75$ (non-fragile). Simulation parameters are listed in the text, and: (a) $\Delta t = 0.9\Delta t_{\text{thresh}} \equiv 0.9\Delta x$; (b) $\Delta t = 0.005 \gtrsim 5\Delta t_{\text{thresh}}$; (c) $\Delta t = 0.2 \gtrsim 200\Delta t_{\text{thresh}}$. Panel (d) is a magnified view of (c), presented in order to show details of the spectrum near the soliton's spectral location. In (a) only, the red curve shows the spectrum of the initial condition. In all figures in Section 3.1 we do not show results for the ψ_2 -component because they are similar to those for the ψ_1 -component.

The purpose of Fig. 2(c) is to present evidence that the stability threshold $\Delta t_{\text{thresh}} = O(\sqrt{\Delta x})$,

stated in Corollary 3.5 of [10], is likely incorrect. Indeed, for $\Delta t = 0.2$ used to obtain Fig. 2(c), $\Delta t/\sqrt{\Delta x} \approx 6.5$, but no trace of exponentially growing harmonics is seen. (It is this ability to have the ratio $\Delta t/\sqrt{\Delta x}$ to significantly exceed 1 that made us choose Δx to be as small as above. Had one not needed to ensure that $\Delta t/\sqrt{\Delta x} > 1$, then a much greater Δx would have sufficed to make the approximation error of the discrete Fourier transform in (10) negligible compared to the splitting error $O(\Delta t^2)$ of the 2nd-order SSM.) While the numeric constant in front of $\Delta t/\sqrt{\Delta x}$ was not specified in [10], it appears to be unlikely that it would be greater than 6.5, as in the case reported in Fig. 2(c).

We will now show that NI near $k_{n\pi}$ *does* occur for $\Delta t > \Delta t_{\text{thresh}}$ if the background soliton is fragile. We illustrate this in Fig. 3 for the soliton with $\Omega = 0.35$ (see Fig. 1). In Fig. 3(a), where $\Delta t < \Delta t_{\text{thresh}}$, the resonant wavenumber k_π is outside the computational domain, and hence no NI can exist near it. The modes which appear at k_{max} (and which we verified to grow exponentially in time) occur there for *any* Δt , no matter how small, and hence are not related to the condition $\Delta t < \Delta t_{\text{thresh}}$. We will discuss them in more detail in Section 3.2. In Fig. 3(b), where $\Delta t > \Delta t_{\text{thresh}}$ and hence $k_\pi < k_{\text{max}}$, one observes two groups of modes on both sides of k_π which grow exponentially in time: see Fig. 3(c). We discuss their relation to (weak) fragility of solitons in Appendix B.

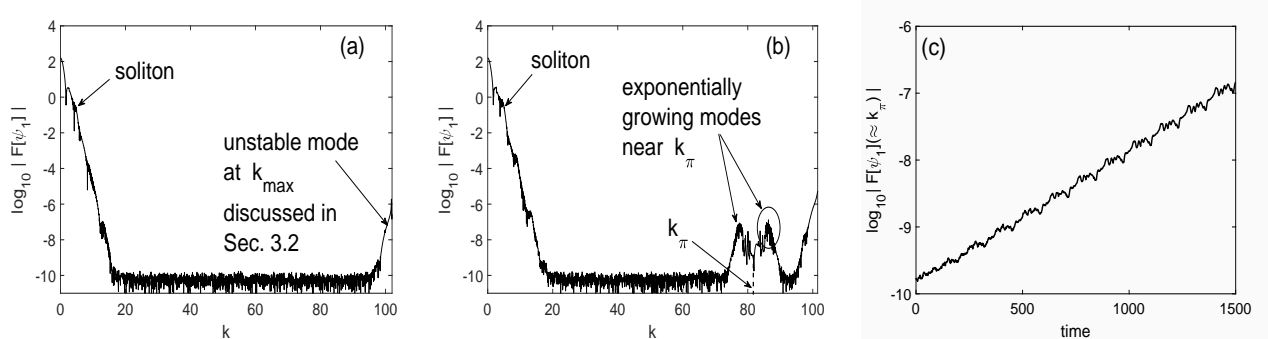


Figure 3: (a,b): Numerical solution’s spectrum for the initial soliton with $\Omega = 0.35$ (fragile). (Only the $k > 0$ part of the spectrum is shown for better visibility of details; the spectrum is symmetric about $k = 0$.) Simulation parameters are: $L = 40\pi$; $N = 2^{12}$, so that $\Delta x \approx 0.031$; $t_{\text{max}} = 1,500$; and: (a) $\Delta t = 0.9\Delta t_{\text{thresh}} \equiv 0.9\Delta x$; (b) $\Delta t = 1.25\Delta t_{\text{thresh}}$. (c) Evolution of the amplitude of the largest mode in the group circled in panel (b).

3.2 Unconditionally unstable modes near edges of spectral domain

As we mentioned in the previous paragraph, the modes referred to in the title of this subsection can be observed when the soliton is fragile. We have verified that, for the parameters of Fig. 3(a), such modes exist for Δt as small as 10^{-4} , i.e. $\Delta t < \Delta x/300$. In the analysis in Section 5 we will show that, indeed, such modes persist for $\Delta t \rightarrow 0$. As Ω increases, the growth rate of these modes decreases, and vice versa. This is illustrated in Fig. 4(a); note the different simulation times.

Applying gentle absorbing boundary conditions, as described in [32], was found to suppress these unstable modes for $\Omega = 0.35$ and 0.50 , but not for 0.20 . This observation is explained by Fig. 4(b), which shows that this mode becomes localized (albeit with slowly decaying ‘tails’) as Ω

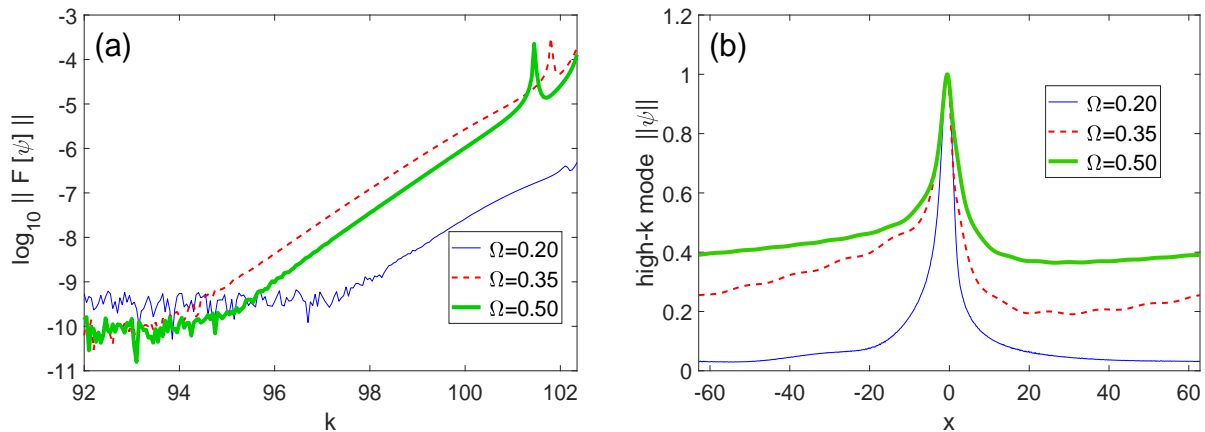


Figure 4: (a) Close-up on the spectrum near k_{\max} . Note that simulation times were different, as follows: $t = 150$ for $\Omega = 0.2$; $t = 1500$ for $\Omega = 0.35$, and $t = 5000$ for $\Omega = 0.5$. Other simulation parameters are: $L = 40\pi$, $N = 2^{12}$ ($\Delta x \approx 0.031$), and $\Delta t = 0.01$. (b) The shape of the unstable modes in the x -domain, extracted from the results reported in (a) with a high-pass filter that extends from $k = 80$ to $k = k_{\max}$. The modes’ amplitudes are normalized to one. The notation $\|\cdots\|$ stands for the ℓ^2 -norm of the corresponding two-component vector.

decreases. Clearly, absorbing boundary conditions can have only a relatively small effect on such a localized mode.

Similarly to the NI for the NLS soliton [16], relatively small variations of L lead to *substantial* changes of the modes’ growth rate. Moreover, they also lead to another unexpected behavior, which, along with the changes mentioned in the previous sentence, is described in the next subsection.

3.3 Unconditionally unstable “noise floor”

The spectrum of the numerical solution in Figs. 2 and 3 away from the soliton looks like a “floor”. It appears approximately level because so is the spectrum of the white noise, which is added to the initial condition in all our simulations. Thus, we will refer to this part of the spectrum as the “noise floor”. In this subsection we present numerical evidence that the “noise floor” *as a whole* can also become unconditionally unstable.

In Fig. 5(a) we show part of the spectrum of the numerical solution for parameters that are similar to those in Fig. 4: $\Omega = 0.35$, $N = 2^{12}$, $\Delta t = 0.01$ ($< \Delta t_{\text{thresh}}/3$), $t = 1500$, and four values of L in the vicinity of 40π . These results demonstrate that relatively small variation of L can suppress the growth of unstable modes near $\pm k_{\max}$ and/or make the “noise floor” unstable. This NI is unconditional: reducing Δt to 0.001 left the results shown in Fig. 5 essentially unchanged. It is also not affected by varying N (for the same L).

In Fig. 5(b) we demonstrate that the “noise floor” NI is exponential. For the purposes of analysis in Section 6 we also show the growth of the same Fourier mode when instead of adding to the initial condition a small white noise, one adds a small constant of the same order of magnitude to each Fourier mode. The analysis forthcoming in Section 6 will explain the observed staircase structure of the dashed curve in Fig. 5(b).

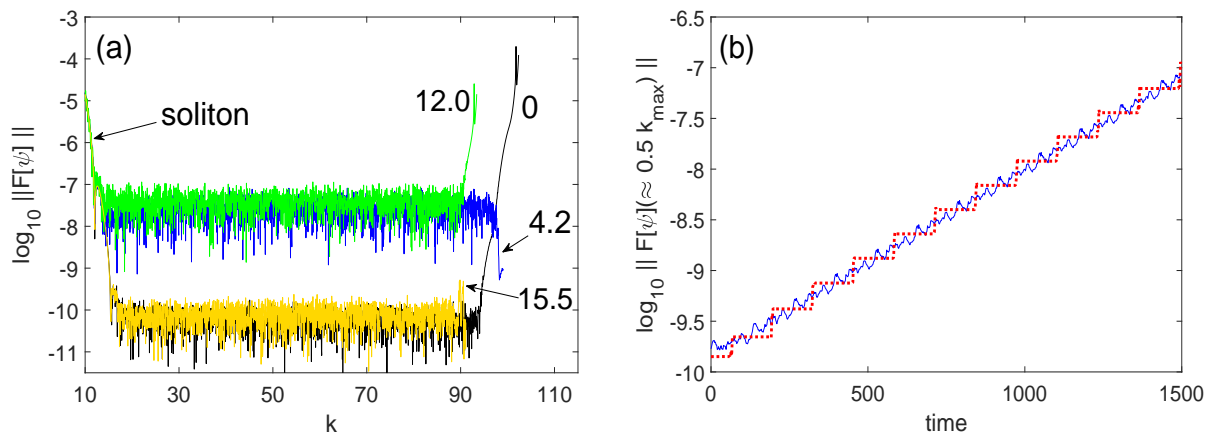


Figure 5: (a) Part of the numerical solution’s spectrum focusing on the “noise floor”. Simulation parameters are listed in the text, and the length of the computational domain is $L = 40\pi + \delta L$, with the value of δL labeling the corresponding curve. Four possible combinations, with the “noise floor” and the modes near k_{\max} being (almost) stable or unstable, are shown. (b) Evolution of the amplitude of the Fourier modes near $k = 60$ for the curve labeled with ‘4.2’ in panel (a). Solid and dashed lines correspond to a small white noise or a constant, respectively, being added to each Fourier mode in the initial condition.

4 Setup of analysis, and dynamics of Fourier modes near $k_{m\pi}$

The main results of this section are Eqs. (25) and (26). They govern the evolution of the Fourier harmonics of a small and spectrally localized perturbation of the soliton with wavenumbers being far from (Eqs. (25)) and near (Eqs. (26)) the resonant wavenumbers (13). Equations (26) explain the numerical observations reported in Section 3.1. Moreover, the derivation steps carried out in this section are later used in the analyses of Sections 5 and 6 for different types of perturbations.

Stability of the second-order SSM (10) is the same as that of the first-order one,

$$\begin{pmatrix} \psi_1 \\ \psi_2 \end{pmatrix} (x, t + \Delta t) = \exp [i(\Delta t)\mathcal{D}] \exp [i\Delta t\mathcal{N}] \begin{pmatrix} \psi_1 \\ \psi_2 \end{pmatrix} (x, t), \quad (14)$$

because in the bulk of the calculation, the first and last $\mathcal{D} \Delta t/2$ -substeps in (10) merge into one $\mathcal{D} \Delta t$ -substep in (14). Therefore, below we study stability of the SSM (14). Stability of a higher-order SSM can differ from that of the first- and second-order SSM [16]; however, this issue is outside the scope of this study.

We will require the definition of an N -point discrete Fourier transform and its inverse:

$$\mathcal{F}[f(x)] \equiv \hat{f}(k_l) = \sum_{j=-N/2}^{N/2-1} f(x_j) e^{-ik_l x_j}; \quad \mathcal{F}^{-1}[\hat{f}(k)] \equiv f(x_j) = \frac{1}{N} \sum_{l=-N/2}^{N/2-1} \hat{f}(k_l) e^{ik_l x_j}, \quad (15)$$

with $k_l = l\Delta k \equiv 2\pi l/L$. Following [16], we consider stability of a numerical perturbation whose spectral content is localized near wavenumbers $\pm k_0$ for some $k_0 \gg 1$, $k_0 \not\approx k_{\max}$. Thus, the solution has the form (7), where the vector $\tilde{\psi}_{\{n\}}(x) \equiv \tilde{\psi}(x, n\Delta t)$, defined after that equation, is sought in the form:

$$\tilde{\psi}_{\{n\}}(x) = \alpha_{\{n\}}(x) e^{ik_0 x} + \beta_{\{n\}}(x) e^{-ik_0 x}. \quad (16)$$

Here we assume that the spectral width of α and β is of order one and hence is much smaller than k_0 ; therefore, the two terms in (16) are well separated in the Fourier space. Note that here and everywhere below, the subscript in curly brackets, such as $\{n\}$, denotes the time level $n\Delta t$, whereas subscripts without curly brackets denote either indices of Fourier harmonics, as in (15), or partial differentiation, as in (1) or (2), depending on the context.

Substitution of (7) and (16) into (14), subsequent linearization, and taking the Fourier transform result in:

$$|k-k_0| = O(1) : \quad \mathcal{F} \left[\alpha_{\{n+1\}} e^{ik_0x} \right] e^{-i\Omega\Delta t} = e^{-i\sigma_1 k \Delta t} \mathcal{F} \left[\alpha_{\{n\}} e^{ik_0x} + i\Delta t \left(P\alpha_{\{n\}} + Q\beta_{\{n\}}^* \right) e^{ik_0x} \right], \quad (17a)$$

$$|k+k_0| = O(1) : \quad \mathcal{F} \left[\beta_{\{n+1\}} e^{-ik_0x} \right] e^{-i\Omega\Delta t} = e^{-i\sigma_1 k \Delta t} \mathcal{F} \left[\beta_{\{n\}} e^{-ik_0x} + i\Delta t \left(P\beta_{\{n\}} + Q\alpha_{\{n\}}^* \right) e^{-ik_0x} \right], \quad (17b)$$

where P and Q are defined in (8), and

$$e^{-i\sigma_1 k \Delta t} \equiv \sigma_0 \cos(k\Delta t) - i\sigma_1 \sin(k\Delta t). \quad (18)$$

Next, in (17a), one writes $\exp[-i\sigma_1 k \Delta t] = \exp[-i\sigma_1 k_0 \Delta t] \exp[-i\sigma_1 (k - k_0) \Delta t]$ and takes the inverse Fourier transform to obtain:

$$\alpha_{\{n+1\}} e^{-i\Omega\Delta t} = e^{-i\sigma_1 k_0 \Delta t} \left(\alpha_{\{n\}} - \Delta t \sigma_1 \alpha_{\{n\},x} + i\Delta t (P\alpha_{\{n\}} + Q\beta_{\{n\}}^*) \right) + O(\Delta t^2). \quad (19a)$$

Indeed, since $|k-k_0|\Delta t \ll 1$, we have approximated $\mathcal{F}^{-1} \left[\exp[-i\sigma_1 (k - k_0) \Delta t] \mathcal{F} \left[\alpha_{\{n\}} \exp[ik_0x] \right] \right]$ by

$$\mathcal{F}^{-1} \left[(\sigma_0 - i\sigma_1 (k - k_0) \Delta t) \mathcal{F} \left[\alpha_{\{n\}} e^{ik_0x} \right] \right] = \alpha_{\{n\}} e^{ik_0x} - \sigma_1 (\partial_x - ik_0) \left(\alpha_{\{n\}} e^{ik_0x} \right) = (\alpha_{\{n\}} - \sigma_1 \alpha_{\{n\},x}) e^{ik_0x}$$

and $\Delta t \exp[-i\sigma_1 (k - k_0) \Delta t]$ by Δt with accuracy $O(\Delta t)$. Similarly, and omitting $O(\Delta t^2)$ terms, one obtains from (17b):

$$\beta_{\{n+1\}} e^{-i\Omega\Delta t} = e^{i\sigma_1 k_0 \Delta t} \left(\beta_{\{n\}} - \Delta t \sigma_1 \beta_{\{n\},x} + i\Delta t (P\beta_{\{n\}} + Q\alpha_{\{n\}}^*) \right). \quad (19b)$$

Since $k_0 \gg 1$, the factors $\exp[\mp i\sigma_1 k_0 \Delta t]$ dominate the evolutions of α_n and β_n . Accordingly, we use the standard perturbation theory approach and seek solutions of (19) in the form:

$$\alpha_{\{n\}} = e^{-in\sigma_1 k_0 \Delta t} \left(\mathbf{a}_{\{n\}}^{(0)} + \mathbf{a}_{\{n\}}^{(1)} \right), \quad \beta_{\{n\}} = e^{in\sigma_1 k_0 \Delta t} \left(\mathbf{b}_{\{n\}}^{(0)} + \mathbf{b}_{\{n\}}^{(1)} \right), \quad (20a)$$

where $\mathbf{a}_{\{n\}}^{(0)}$, $\mathbf{b}_{\{n\}}^{(0)}$ vary with n slowly compared to $\exp[\mp in\sigma_1 k_0 \Delta t]$, and

$$\left\{ |\mathbf{a}_{\{n\}}^{(1)}|, |\mathbf{b}_{\{n\}}^{(1)}| \right\} = O \left(\Delta t \cdot \left\{ |\mathbf{a}_{\{n\}}^{(0)}|, |\mathbf{b}_{\{n\}}^{(0)}| \right\} \right) \quad \forall n. \quad (20b)$$

Substituting (20) into (19a), multiplying both sides by $\exp[i(n+1)\sigma_1 k_0 \Delta t]$, and again discarding $O(\Delta t^2)$ terms, one has:

$$\begin{aligned} \mathbf{a}_{\{n+1\}}^{(0)} (1 - i\Omega\Delta t) + \mathbf{a}_{\{n+1\}}^{(1)} &= \mathbf{a}_{\{n\}}^{(0)} - \Delta t \sigma_1 \mathbf{a}_{\{n\},x}^{(0)} + \mathbf{a}_{\{n\}}^{(1)} + \\ i\Delta t \left[\left(P_{01} + e^{2i(n+1)\sigma_1 k_0 \Delta t} P_{23} \right) \mathbf{a}_{\{n\}}^{(0)} + \left(Q_{01} + e^{2i(n+1)\sigma_1 k_0 \Delta t} Q_{23} \right) (\mathbf{b}_{\{n\}}^{(0)})^* \right]. \end{aligned} \quad (21)$$

Here $\mathbf{P}_{jl} \equiv \sigma_j P_j + \sigma_l P_l$ and similarly for \mathbf{Q}_{jl} , and we have used the identity

$$e^{i\sigma_1 s} \sigma_j e^{-i\sigma_1 s} = e^{2i\sigma_1 s} \sigma_j, \quad j = 2, 3, \quad (22)$$

which follows from the anti-commutation of σ_1 with $\sigma_{2,3}$. A similar equation holds for $\mathbf{b}^{(0),(1)}$.

Subsequent analysis of these equations depends on whether $k_0 \approx k_{m\pi}$ for some $m \in \mathbb{N}$. To set up analyses in Sections 5 and 6, we first consider the case where $k_0 \neq k_{m\pi}$ (i.e., $|k_0 - k_{m\pi}| \gg 1$). Then terms in (21) which are proportional to $\mathbf{a}^{(0)}$ and $(\mathbf{b}^{(0)})^*$ split into two groups: fast-oscillating (proportional to $\exp[2i(n+1)\sigma_1 k_0 \Delta t]$) and those varying slowly with n . If the latter terms do not all cancel out, they will drive the $\mathbf{a}_{\{n\}}^{(1)}$ -term, which therefore will grow, and condition (20b) will eventually be violated. To prevent this from occurring, one requires that all these slowly varying terms cancel out, yielding:

$$\mathbf{a}_{\{n+1\}}^{(0)}(1 - i\Omega\Delta t) = (\sigma_0 - \Delta t \sigma_1 \partial_x) \mathbf{a}_{\{n\}}^{(0)} + i\Delta t \left(\mathbf{P}_{01} \mathbf{a}_{\{n\}}^{(0)} + \mathbf{Q}_{01} (\mathbf{b}_{\{n\}}^{(0)})^* \right). \quad (23a)$$

The remaining terms provide an equation for $\mathbf{a}^{(1)}$:

$$\mathbf{a}_{\{n+1\}}^{(1)} - \mathbf{a}_{\{n\}}^{(1)} = \Delta t e^{2i(n+1)\sigma_1 k_0 \Delta t} \mathbf{c}_{\{n\}}, \quad \mathbf{c}_{\{n\}} \equiv \mathbf{P}_{23} \mathbf{a}_{\{n\}}^{(0)} + \mathbf{Q}_{23} (\mathbf{b}_{\{n\}}^{(0)})^*; \quad (23b)$$

note that $\mathbf{c}_{\{n\}}$ varies slowly with n . Due to this fact and the presence of a fast-varying exponential on the r.h.s. of (23b), the solution of that equation does not grow with n , and hence condition (20b) holds. Thus, since the terms $\mathbf{a}^{(1)}$, $\mathbf{b}^{(1)}$ remain small compared to $\mathbf{a}^{(0)}$, $\mathbf{b}^{(0)}$ at all times, we will no longer consider the former terms and will focus on the latter. Taking into account the slow dependence of $\mathbf{a}_{\{n\}}^{(0)}$ on n , we approximate

$$\mathbf{a}_{\{n+1\}}^{(0)} = \mathbf{a}_{\{n\}}^{(0)} + \Delta t (\partial_t \mathbf{a}^{(0)})_{\{n\}} + O(\Delta t^2). \quad (24)$$

Finally, substituting (24) into (23a) and omitting (Δt^2) terms, we obtain:

$$\mathbf{a}_t + \sigma_1 \mathbf{a}_x - i\Omega \mathbf{a} = i\mathbf{P}_{01} \mathbf{a} + i\mathbf{Q}_{01} \mathbf{b}^*. \quad (25a)$$

Here and below we will omit the superscript (0) of \mathbf{a} and \mathbf{b} . Similar calculations yield the equation for \mathbf{b} :

$$\mathbf{b}_t + \sigma_1 \mathbf{b}_x - i\Omega \mathbf{b} = i\mathbf{Q}_{01} \mathbf{a}^* + i\mathbf{P}_{01} \mathbf{b}. \quad (25b)$$

We will return to the derivation in this paragraph in Sections 5 and 6.

Now, in the case $k_0 = k_{m\pi}$, since $2k_0 \Delta t = 2m\pi$, all terms in (21) vary slowly with n . (This also holds for $|k_0 - k_{m\pi}| = O(1)$, since we can use the freedom in (16), which requires only that α and β vary in x on the scale of order one.) Following the derivation in the previous paragraph, one obtains, instead of (25), equations:

$$\mathbf{a}_t + \sigma_1 \mathbf{a}_x - i\Omega \mathbf{a} = i\mathbf{P} \mathbf{a} + i\mathbf{Q} \mathbf{b}^*. \quad (26a)$$

$$\mathbf{b}_t + \sigma_1 \mathbf{b}_x - i\Omega \mathbf{b} = i\mathbf{Q} \mathbf{a}^* + i\mathbf{P} \mathbf{b}. \quad (26b)$$

Thus, vector $(\mathbf{a}^T, (\mathbf{b}^*)^T)^T$, representing a perturbation that is spectrally localized near $k_{m\pi}$, satisfies the same equation (9) that governs the evolution of a low- k perturbation to the soliton. Therefore, modes near $k_{m\pi}$ have the same stability properties as the low-wavenumber modes. In other words, NI near $k_{m\pi}$ occurs if and only if low- k perturbations of the soliton grow exponentially. Thus, the above analysis has explained the numerical observations of Section 3.1 and Appendix B.

5 Unconditional numerical instability near $|k| = k_{\max}$

In this section we will present a theory explaining the numerical results of Section 3.2. This will be accomplished by numerically solving the eigenvalue problem (33).

A numerical perturbation whose spectral content is concentrated near the edges of the computational domain is sought in the form (16), where now $k_0 = k_{\max}$ and, in addition, the Fourier transform of $\alpha(x)$ (of $\beta(x)$) contains harmonics with only negative (respectively, nonnegative) wavenumbers:

$$\alpha(x) = \sum_{l=1}^M \hat{\alpha}_l e^{-ik_l x}, \quad \beta(x) = e^{-i\Delta k x} \sum_{l=1}^M \hat{\beta}_l e^{ik_l x}, \quad (27)$$

where $1 \ll M \ll N/2$. The last strong inequality holds because the spectral content of the perturbation is concentrated near the edges of the spectral domain. Recall that the computational spectral window is $k_l \in [-k_{\max}, k_{\max} - \Delta k]$, where k_{\max} is defined in (4c) and $k_l, \Delta k$ are defined after (15).

When we substitute Eqs. (16) with (27) into (14), then, similarly to the r.h.s. of (17), we obtain terms like $\mathbf{P}\alpha \exp[ik_{\max}x]$ etc.. Note, however, that the coefficient $\mathbf{P}(x)\alpha(x)$ had Fourier harmonics with wavenumbers of both signs, due to $\mathbf{P}(x)$ having such harmonics. Therefore, such terms are to be split into two groups:

$$\mathbf{P}\alpha \equiv [\mathbf{P}\alpha]^{(<0)} + [\mathbf{P}\alpha]^{(\geq 0)}, \quad (28a)$$

where the superscript indicates what Fourier harmonics the term has. When multiplied by $\exp[ik_{\max}x]$, the former group of terms on the r.h.s. of (28a) will have the spectral content near the right edge of the spectral domain, while the latter group's spectral content will "spill over" to the left edge due to aliasing. Thus,

$$\mathbf{P}\alpha e^{ik_{\max}x} = [\mathbf{P}\alpha]^{(<0)} e^{ik_{\max}x} + [\mathbf{P}\alpha]^{(\geq 0)} e^{-ik_{\max}x}. \quad (28b)$$

With this observation in mind, the counterparts of Eqs. (17) near the edges of the spectral domain become:

$$\hat{\alpha}_{\{n+1\}} e^{i\sigma_1(k_{\max} + \delta k^{(<0)})\Delta t - i\Omega\Delta t} = \hat{\alpha}_{\{n\}} + i\Delta t \mathcal{F} \left[\left[\mathbf{P}(\alpha_{\{n\}} + \beta_{\{n\}}) + \mathbf{Q}(\alpha_{\{n\}}^* + \beta_{\{n\}}^*) \right]^{(<0)} \right], \quad (29a)$$

$$\hat{\beta}_{\{n+1\}} e^{i\sigma_1(-k_{\max} + \delta k^{(\geq 0)})\Delta t - i\Omega\Delta t} = \hat{\beta}_{\{n\}} + i\Delta t \mathcal{F} \left[\left[\mathbf{P}(\alpha_{\{n\}} + \beta_{\{n\}}) + \mathbf{Q}(\alpha_{\{n\}}^* + \beta_{\{n\}}^*) \right]^{(\geq 0)} \right], \quad (29b)$$

where

$$\delta k^{(<0)} = k - k_{\max} < 0, \quad \delta k^{(\geq 0)} = k + k_{\max} \geq 0.$$

Note that all Fourier transforms in (29a) (in (29b)) are evaluated at $\delta k^{(<0)}$ (respectively, at $\delta k^{(\geq 0)}$).

In Section 4 we were able to take the inverse Fourier transform of Eqs. (17), which are counterparts of Eqs. (29), and proceed with the analysis in the x -space. In the case of Eqs. (29), this would result not in differential equations, such as (25) or (26), but in integro-differential ones, due to the separation of positive and negative wavenumbers on the r.h.s. of (29). Quantitative analysis of such integro-differential equations would be more difficult than analysis of the original Fourier-space equations (29). Therefore, below we will proceed with the latter analysis.

Following the derivation of Eqs. (25), except for not taking the inverse Fourier transform, one obtains from (29):

$$\widehat{\mathbf{a}}_t = i \left(\sigma_0 \Omega - \sigma_1 \delta k^{(<0)} \right) \widehat{\mathbf{a}} + i \mathcal{F} \left[[\mathbf{P}_{01} \mathbf{a} + \mathbf{P}_{23} \mathbf{b} + \mathbf{Q}_{23} \mathbf{a}^* + \mathbf{Q}_{01} \mathbf{b}^*]^{(<0)} \right], \quad (30a)$$

$$\widehat{\mathbf{b}}_t = i \left(\sigma_0 \Omega - \sigma_1 \delta k^{(\geq 0)} \right) \widehat{\mathbf{b}} + i \mathcal{F} \left[[\mathbf{P}_{23} \mathbf{a} + \mathbf{P}_{01} \mathbf{b} + \mathbf{Q}_{01} \mathbf{a}^* + \mathbf{Q}_{23} \mathbf{b}^*]^{(\geq 0)} \right]. \quad (30b)$$

Using the same justification as in (25), we have neglected small terms $\widehat{\mathbf{a}}^{(1)}$, $\widehat{\mathbf{b}}^{(1)}$ and omitted the superscript (0). System (30) determines stability of a $8M$ -dimensional vector: M harmonics in each of the two-component vectors $\widehat{\mathbf{a}}$ and $\widehat{\mathbf{b}}$ are coupled with as many harmonics of their complex conjugates. It is possible to halve the size of the involved vectors (i.e., from $8M$ to $4M$) by means of the following substitution:

$$\widehat{\mathbf{a}} = \widehat{a}_{(+)} \mathbf{e}_{(+)} + \widehat{a}_{(-)} \mathbf{e}_{(-)}, \quad \widehat{\mathbf{b}} = \widehat{b}_{(+)} \mathbf{e}_{(+)} + \widehat{b}_{(-)} \mathbf{e}_{(-)}, \quad \mathbf{e}_{(\pm)} \equiv \begin{pmatrix} 1 \\ \pm 1 \end{pmatrix}; \quad (31)$$

the same decomposition also holds for \mathbf{a} and \mathbf{b} . Vectors $\mathbf{e}_{(\pm)}$ satisfy the following relations:

$$\sigma_0 \mathbf{e}_{(\pm)} = \mathbf{e}_{(\pm)}, \quad \sigma_1 \mathbf{e}_{(\pm)} = \pm \mathbf{e}_{(\pm)}, \quad \sigma_2 \mathbf{e}_{(\pm)} = \mp i \mathbf{e}_{(\mp)}, \quad \sigma_3 \mathbf{e}_{(\pm)} = \mathbf{e}_{(\mp)}. \quad (32)$$

The resulting equations, which couple harmonics $\widehat{a}_{(+)}$, $\widehat{b}_{(-)}$, $\widehat{a}_{(-)}$, $\widehat{b}_{(+)}$, are found in Appendix C. Here we present only their matrix form, which is needed for a stability analysis. Defining M -dimensional column vectors, e.g.: $\underline{\widehat{a}}_{(+)} = [(\widehat{a}_{(+)})_1, \dots, (\widehat{a}_{(+)})_M]^T$, etc., where the numeric subscript denotes the harmonic's number (see (27)) and 'T' denotes the transpose, one can write system (C.1) as:

$$\underline{\mathbf{x}}_t = i (\mathbb{D} + \mathbb{C}) \underline{\mathbf{x}}, \quad (33a)$$

where:

$$\mathbb{D} = \begin{pmatrix} \Delta k \mathbb{M} + \Omega \mathbb{I} & 0 & 0 & 0 \\ 0 & \Delta k (\mathbb{M} - \mathbb{I}) + \Omega \mathbb{I} & 0 & 0 \\ 0 & 0 & \Delta k \mathbb{M} - \Omega \mathbb{I} & 0 \\ 0 & 0 & 0 & \Delta k (\mathbb{M} - \mathbb{I}) - \Omega \mathbb{I} \end{pmatrix}, \quad (33b)$$

$$\underline{\mathbb{I}}\underline{\mathbb{a}} = \begin{pmatrix} \widehat{\underline{a}}_{(+)} \\ \widehat{\underline{b}}_{(-)} \\ \widehat{\underline{a}}_{(-)}^* \\ \widehat{\underline{b}}_{(+)}^* \end{pmatrix}, \quad \mathbb{C} = \frac{1}{N} \begin{pmatrix} \mathbb{C}_{11} & \mathbb{C}_{12} & \mathbb{C}_{13} & \mathbb{C}_{14} \\ \mathbb{C}_{21} & \mathbb{C}_{22} & \mathbb{C}_{23} & \mathbb{C}_{24} \\ \mathbb{C}_{31} & \mathbb{C}_{32} & \mathbb{C}_{33} & \mathbb{C}_{34} \\ \mathbb{C}_{41} & \mathbb{C}_{42} & \mathbb{C}_{43} & \mathbb{C}_{44} \end{pmatrix}, \quad (33c)$$

N is the total number of grid points in the computational domain (see (15)); \mathbb{I} is the $M \times M$ identity matrix; $\mathbb{M} = \text{diag}[1 : M]$ is the $M \times M$ diagonal matrix with integer entries; and the $M \times M$ blocks \mathbb{C}_{jm} , which appear from the convolution-like terms on the r.h.s. of (30), are written out explicitly in Appendix C. Each of these blocks has a logically clear structure and can be easily programmed.

The stability analysis of system (33) is straightforward: one seeks $\underline{\mathbb{a}}$ proportional to $\exp[\lambda t]$, whence the system becomes a $4M \times 4M$ eigenvalue problem. For $M \sim 100$, it is solved by Matlab in about 1 second. Eigenvalues with $\text{Re}\lambda > 0$ correspond to numerically unstable modes, which, by design, occur near the edges of the computational spectrum. In Fig. 6 we show the unstable eigenvectors of that system corresponding to the solitons with the three values of Ω for which graphs are shown in Fig. 4(a). One can see a good agreement between the spectral profiles of the unstable modes in that figure and their counterparts in Fig. 6(d)–(f). Furthermore, in Fig. 7 we show the NI growth rate (i.e., $\max \text{Re}\lambda$) versus the length L of the computational domain for the same three values of Ω . The values obtained from the preceding analysis match closely the corresponding values measured in direct numerical simulations, thus *validating our analysis*.

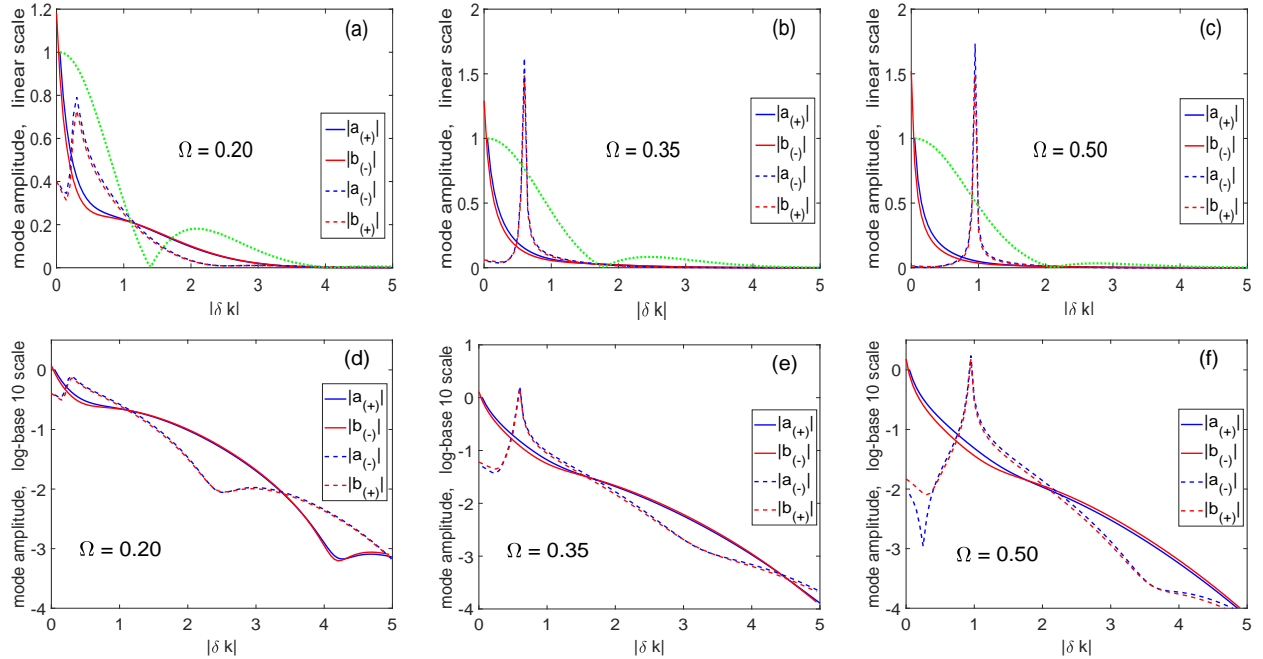


Figure 6: (Color online) Shapes of the most unstable eigenvectors of (33), $|\widehat{\underline{a}}_{(\pm)}|$ vs. $\delta k^{(<0)}$ and $|\widehat{\underline{b}}_{(\pm)}|$ vs. $\delta k^{(\geq 0)}$, for the solitons with the same values of Ω as shown in Fig. 4(a). Panels (a)–(c): linear scale; panels (d)–(f): logarithmic scale. All eigenvectors are normalized to $\max |\widehat{\underline{a}}_{(+)}|$. In (a)–(c), the dotted green line shows $\widehat{P}_0(k)$, normalized to 1, for comparison.

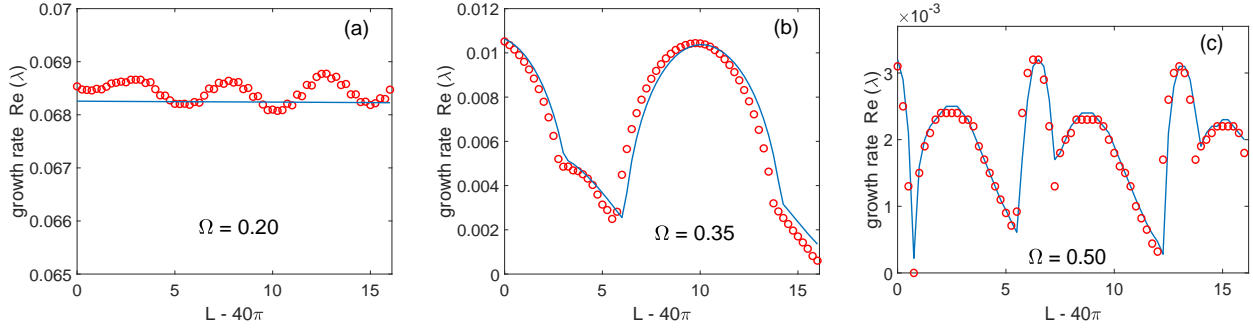


Figure 7: Growth rate of the most unstable mode of eigenvalue problem (33) as the function of length L of the computational domain. Note that the vertical scales are drastically different in all three panels. Solid lines correspond to the solution of (33), while circles are the result of simulations by the SSM.

Two clarifications about Fig. 7 are in order. First, the dependence of the eigensolutions of problem (33) on L occur only via $\Delta k = 2\pi/L$. Second, the growth rate deduced from direct numerical simulations was computed as follows. For a given Ω , the simulations were run up to the respective time indicated in the caption to Fig. 4. The temporal evolution of the logarithm of the maximum amplitude of Fourier harmonics in some vicinity of $k = k_{\max}$ was plotted, as in Fig. 3(c). The growth rate was deduced from the slope of the linear part of that graph.

In Fig. 8(a) we show the NI growth rate as a function of L of a non-fragile soliton with $\Omega = 0.75$. Again, a good agreement between our analysis and direct numerics is seen. Thus, the SSM can be unconditionally unstable even for non-fragile solitons; it is just that in that case, the instability is so weak that it will not affect simulations for most realistic simulation times.

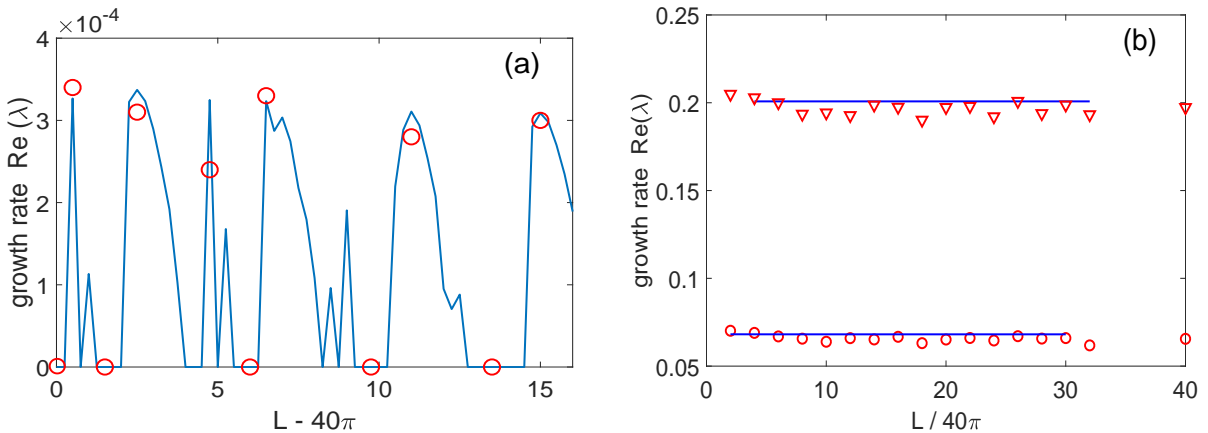


Figure 8: Growth rate of the most unstable mode at the spectral edges as the function of length L of the computational domain. Note that *both* vertical and horizontal scales are drastically different in panels (a) and (b). Solid line: solution of (33). Symbols: simulations by the SSM with $\Delta t = \Delta x/5$. Panel (a): $\Omega = 0.75$, $N = 2^{12}$, and $t = 50,000$. Because of the large simulation time, which in turn is due to a very small growth rate, simulations were run only for the major “peaks” and for the midpoints of the intervals where the theory predicts zero growth rate. Panel (b): $\Omega = 0.2$ and 0.1 . Simulations by the SSM were run to $t = 300$ (circles) and 150 (triangles), respectively. Number of grid points was adjusted as $N = 2^{12} L/(40\pi)$.

Finally, in Fig. 8(b) we expand on the trend which may already be noticed from Fig. 7(a). Namely, for sufficiently small Ω , the growth rate of the unstable modes near $\pm k_{\max}$ is nearly independent of the length of the computational domain. We will discuss this further in Section 8.

6 Unconditional instability of the “noise floor”

The main result of this section is based on Eq. (44), which describes the evolution of the “noise floor” amplitude. The growth rate of the “noise floor” is found from the spectral radius of the corresponding fundamental solution, defined in (45b).

To study the “noise floor” NI, described in Section 3.3 and illustrated in Fig. 5, one cannot use ansatz (16). Indeed, a perturbation described by the “noise floor” is not spectrally narrow and hence is not a slowly-modulated plane wave in the x -space; see the sentence after (16). Instead, we will consider the most general form of a perturbation:

$$\tilde{\psi}_{\{n\}}(x) = \sum_j \hat{\alpha}_{j,\{n\}} e^{ik_j x} + \hat{\beta}_{j,\{n\}} e^{-ik_j x}, \quad (34a)$$

where the double subscript in (34) stands for a Fourier harmonic at wavenumber k_j and time level $n\Delta t$; a similar notation will be employed below in this section. The summation here is assumed over the harmonics of the “noise floor”, i.e. those with

$$k_j \gg 1 \quad \text{and} \quad (k_{\max} - k_j) \gg 1. \quad (34b)$$

The first inequality in (34b) ensures that the harmonics are outside the spectrum of the background soliton, whereas the second one ensures that they are sufficiently far from the edges of the spectral domain. While the derivation of the equations predicting unstable dynamics of $\hat{\alpha}_j$ and $\hat{\beta}_j$ will generally follow the derivation of Section 4, we will specifically emphasize places where key differences occur.

Substituting (7) and (34) into (14) and linearizing, one obtains equations analogous to (17):

$$\hat{\alpha}_{j,\{n+1\}} e^{-i\Omega\Delta t} = e^{-ik_j\sigma_1\Delta t} \left(\hat{\alpha}_{j,\{n\}} + \frac{i\Delta t}{N} \sum_l \hat{P}_l \hat{\alpha}_{j-l,\{n\}} + \hat{Q}_l (\hat{\beta}_{j-l,\{n\}})^* \right), \quad (35a)$$

$$\hat{\beta}_{j,\{n+1\}} e^{-i\Omega\Delta t} = e^{ik_j\sigma_1\Delta t} \left(\hat{\beta}_{j,\{n\}} + \frac{i\Delta t}{N} \sum_l \hat{Q}_l (\hat{\alpha}_{j+l,\{n\}})^* + \hat{P}_l \hat{\beta}_{j+l,\{n\}} \right). \quad (35b)$$

The sums on the r.h.s. of these equations were obtained similarly to those in (C.2) and (C.4); however, for a reason that will become clear soon, the indices were switched between the \hat{P}, \hat{Q} and the $\hat{\alpha}, \hat{\beta}$ terms in (35) compared to those in (C.2) and (C.4). Since the spectral width of the background soliton is $O(1)$, the sum in (35) contains only $O(1)/\Delta k \ll N$ terms that are significantly different from zero.

Similarly to (20), one seeks

$$\hat{\alpha}_{j,\{n\}} = e^{-in\sigma_1 k_j \Delta t} \left(\hat{\mathbf{a}}_{j,\{n\}}^{(0)} + \hat{\mathbf{a}}_{j,\{n\}}^{(1)} \right), \quad \hat{\beta}_{j,\{n\}} = e^{in\sigma_1 k_j \Delta t} \left(\hat{\mathbf{b}}_{j,\{n\}}^{(0)} + \hat{\mathbf{b}}_{j,\{n\}}^{(1)} \right), \quad (36)$$

where the quantities with superscript ‘(0)’ vary slowly in time and those with superscript ‘(1)’ are small. Note, however, that the time dependence explicitly stated in (36) is different from that in (20). In the latter case, since the perturbation $\tilde{\psi}(x)$ was spectrally localized near some wavenumber k_0 , it was appropriate to assume that in the main order, all harmonics evolved proportionally to the same factor, either $\exp[-in\sigma_1 k_0 \Delta t]$ or $\exp[in\sigma_1 k_0 \Delta t]$. On the other hand, since the perturbation (34), considered in this section, is *not* spectrally localized, then the principal evolution of each Fourier harmonic followed its individual exponential, $\exp[\mp in\sigma_1 k_j \Delta t]$. A consequence of this difference will appear in the subsequent derivation.

When one substitutes (36) into (35), one obtains, similarly to (21), two distinct groups of oscillating terms. For example, the $\widehat{P}_l \widehat{\alpha}_{j-l, \{n\}}$ term yields:

$$e^{in\sigma_1 k_j n \Delta t} \widehat{P}_l \widehat{\alpha}_{j-l, \{n\}} = \left(\widehat{P}_{01} e^{in\sigma_1 k_l n \Delta t} + \widehat{P}_{23} e^{in\sigma_1 (k_l - 2k_j) n \Delta t} \right) \left(\widehat{\alpha}_{j-l, \{n\}}^{(0)} + \widehat{\alpha}_{j-l, \{n\}}^{(1)} \right). \quad (37)$$

The terms in the first group on the r.h.s. vary on the time scale of order $O(1)$ (see the second sentence after (35)), while the terms in the second group vary much faster due to the first inequality in (34b).¹ Then, arguing as in the paragraph surrounding Eqs. (23), one shows that the rapidly oscillating terms affect only the small corrections $\widehat{\alpha}_{j, \{n\}}^{(1)}$, $\widehat{\mathbf{b}}_{j, \{n\}}^{(1)}$, but in the main order do not contribute to the evolution of the principal terms $\widehat{\alpha}_{j, \{n\}}^{(0)}$, $\widehat{\mathbf{b}}_{j, \{n\}}^{(0)}$. Therefore, in what follows we omit those rapidly oscillating terms and will also omit the superscript (0), as done after (24). Following the above steps and also approximating the finite differences in time with time derivatives, as done in obtaining (30) from (29), we find:

$$(\widehat{\alpha}_j)_t = i\Omega \widehat{\alpha}_j + \frac{i}{N} \sum_l \widehat{P}_{01} e^{i\sigma_1 k_l t} \widehat{\alpha}_{j-l} + \widehat{Q}_{01} e^{i\sigma_1 k_l t} (\widehat{\mathbf{b}}_{j-l})^*, \quad (38a)$$

$$(\widehat{\mathbf{b}}_j)_t^* = -i\Omega (\widehat{\mathbf{b}}_j)^* - \frac{i}{N} \sum_l \widehat{Q}_{01}^* e^{-i\sigma_1 k_l t} \widehat{\alpha}_{j+l} + \widehat{P}_{01}^* e^{-i\sigma_1 k_l t} (\widehat{\mathbf{b}}_{j+l})^*, \quad (38b)$$

where $t \equiv n\Delta t$.

Exact solution of system (38) would be possible only by direct numerical simulations. Not only would such an approach not be illuminating in any respect, but it would also be considerably more difficult than solving (30) (or, equivalently, (33)), despite the latter equation appearing to have more terms. Indeed, (38), unlike (30), has time-dependent terms on the r.h.s., which is the consequence of the difference between (36) and (20), emphasized after (36). Even more importantly, the system in (38) couples, by virtue of (34b), a much greater number of Fourier harmonics, $\lesssim N/2$ instead of $M \ll N/2$. For these reasons, below we will use a *simplified approach*. It will still require a numerical solution, but only of a 2×2 system. More importantly, it will allow us to *explain the mechanism* by which harmonics of the “noise floor” can become unstable.

The simplification occurs from an observation that none of the coefficients of terms $\widehat{\alpha}$ and $\widehat{\mathbf{b}}$ on the r.h.s. of (38) depends on the harmonic’s index j . Therefore, these equations will be satisfied

¹ Note that since we intend to investigate an unconditional numerical instability, one can consider the limit $\Delta t \rightarrow 0$, and thus there can be no resonances like (13), because of which any of the terms from the second group may become slowly varying.

by a j -independent ansatz:

$$\widehat{\mathbf{a}}_j \equiv \widehat{\mathbf{a}}, \quad \widehat{\mathbf{a}}_j \equiv \widehat{\mathbf{b}} \quad \text{for all } j \text{ satisfying (34b)}. \quad (39)$$

We will come back to interpretation of this ansatz later in this Section. We now expand $\widehat{\mathbf{a}}$ and $\widehat{\mathbf{b}}$ using (31), substitute the result into (38) and collect the scalar coefficients of vectors $\mathbf{e}_{(\pm)}$. For example, the coefficients at $\mathbf{e}_{(+)}$ yield:

$$(\widehat{\mathbf{a}}_{(+)})_t = i\Omega\widehat{\mathbf{a}}_{(+)} + \frac{i}{N} \sum_l \widehat{P}_{0l} e^{ik_l t} \widehat{\mathbf{a}}_{(+)} + \left(\widehat{Q}_{0l} + \widehat{Q}_{1l} \right) e^{ik_l t} (\widehat{\mathbf{b}}_{(+)})^*, \quad (40a)$$

$$(\widehat{\mathbf{b}}_{(+)})_t^* = -i\Omega(\widehat{\mathbf{b}}_{(+)})^* - \frac{i}{N} \sum_l \left(\widehat{Q}_{0l}^* + \widehat{Q}_{1l}^* \right) e^{-ik_l t} \widehat{\mathbf{a}}_{(+)} + \widehat{P}_{0l}^* e^{-ik_l t} (\widehat{\mathbf{b}}_{(+)})^*, \quad (40b)$$

where we have used that $P_1 \equiv 0$. In deriving (40) we have also used the first two of identities (32) as well as the identity

$$e^{i\sigma_1 k_l t} \mathbf{e}_{(\pm)} = e^{\pm ik_l t} \mathbf{e}_{(\pm)}, \quad (41)$$

which follows from (18) and (32). Note that unlike in (33), terms $\widehat{\mathbf{a}}_{(+)}, \widehat{\mathbf{b}}_{(+)}$ are not coupled with $\widehat{\mathbf{a}}_{(-)}, \widehat{\mathbf{b}}_{(-)}$ due to the absence of matrices σ_2, σ_3 in (38).

Here comes the next *key step* in this analysis: we recognize the sums in (40) as the inverse Fourier transform (15) (but in t , not in x), upon which we rewrite Eqs. (40) and their counterparts obtained for $\widehat{\mathbf{a}}_{(-)}, \widehat{\mathbf{b}}_{(-)}$ as:

$$(\mathbf{c}_{(\pm)})_t = \mathbf{R}_{(\pm)} \mathbf{c}_{(\pm)}, \quad (42a)$$

where:

$$\mathbf{c}_{(\pm)} = \begin{pmatrix} \widehat{\mathbf{a}}_{(\pm)} \\ (\widehat{\mathbf{b}}_{(\pm)})^* \end{pmatrix}, \quad \mathbf{R}_{(\pm)} = i\sigma_3 \left(\Omega\sigma_0 + \begin{pmatrix} P_0(\pm t) & Q_0(\pm t) \pm Q_1(\pm t) \\ Q_0^*(\pm t) \pm Q_1^*(\pm t) & P_0^*(\pm t) \end{pmatrix} \right). \quad (42b)$$

Two remarks about the entries of the last matrix in (42b) are in order, both of which are consequence of the difference emphasized after Eqs. (36). First, while P_0 etc. were defined in (8) as functions of x , in the above system they are functions of time. Second, due to the periodicity of discrete Fourier transform, these entries are *periodic*, with the period being L , the length of the computational domain. Thus, although in (42a), $t \in [0, \infty)$, one also requires that

$$P_0(t+L) = P_0(t), \quad Q_{0,1}(t+L) = Q_{0,1}(t) \quad \forall t. \quad (42c)$$

Before we discuss the solution of (42), let us point out that we need to solve *only one*, not two, systems. This follows from the parity properties implied by (8) and (5):

$$P_0(-t) = P_0(t), \quad Q_0(-t) = Q_0(t), \quad Q_1(-t) = -Q_1(t), \quad (43)$$

whence $\mathbf{R}_{(-)} = \mathbf{R}_{(+)}$. Therefore, below we will omit the subscripts ‘ (\pm) ’ of \mathbf{c} and \mathbf{R} . As yet another simplification, we note that $P_0^* = P_0$, $Q_0^* = Q_0$, while $Q_1^* = -Q_1$. Finally, using the explicit form

(8)(c,d) of P_0, Q_0, Q_1 , we can rewrite (42) as:

$$\mathbf{c}_t = i\sigma_3 \left(\Omega\sigma_0 + \frac{1}{2} \begin{pmatrix} \Psi_1^2 - \Psi_2^2 & (\Psi_1 + \Psi_2)^2 \\ (\Psi_1 - \Psi_2)^2 & \Psi_1^2 - \Psi_2^2 \end{pmatrix} \right) \mathbf{c}. \quad (44)$$

Recall that here, $\Psi_{1,2}$ are L -periodic functions of time. Then,

$$\|\mathbf{c}(t)\| \leq \|\Phi(L)\|^{t/L} \|\mathbf{c}(0)\|, \quad t = \text{integer} \cdot L, \quad (45a)$$

where $\|\dots\|$ denotes the ℓ^2 -norm, and the fundamental solution $\Phi(L)$ of (44) satisfies

$$\mathbf{c}(L) = \Phi(L) \mathbf{c}(0). \quad (45b)$$

We are now ready to interpret the meaning of ansatz (39). A perturbation (34) where amplitudes of the harmonics satisfy (39) is approximately² the sum of *two* delta functions in space, where the ‘two’ occurs due to (31) having two contributions, from $\mathbf{e}_{(+)}$ and $\mathbf{e}_{(-)}$. By virtue of (36), these two spikes move with speed 1 in opposite directions. Due to the periodicity of the boundary conditions, they repeatedly leave and re-enter the computational domain. Their amplitudes are changed when they pass through the soliton and remain constant far from the soliton; this follows from (44). If those amplitude changes from consecutive passages are accumulated, the amplitude of the ‘noise floor’ increases; see the dashed line in Fig. 5(b) and Fig. 9(a). When the initial ‘noise floor’ consists of white noise as opposed to the simplified ansatz (39), the above interpretation no longer applies in the exact sense. However, the mechanism of the instability of the ‘noise floor’ is the same: the perturbation (34) repeatedly passes through the soliton, and when L is such that changes of its amplitude over consecutive passages accumulate, the perturbation grows on average exponentially. When they do not, ‘noise floor’'s amplitude oscillates in time (Figs. 9(b,c)). The fact that the evolution of the ‘simplified’ perturbation (34), (39) is predictive of that of the generic perturbation is seen in Figs. 5(b) and 9.

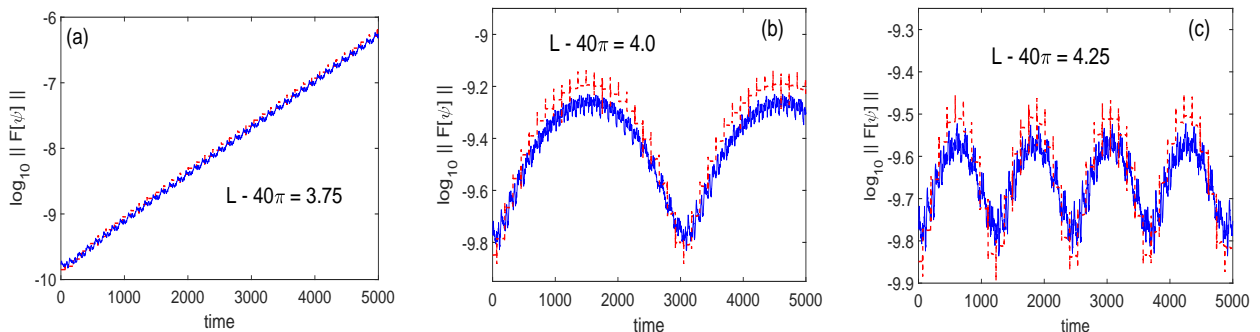


Figure 9: Evolution of the amplitude of harmonics of the ‘noise floor’, similar to that shown in Fig. 5(b), but for $\Omega = 0.50$ and the three values of L indicated in the panels. Solid and dashed lines correspond to a small white noise or a constant, respectively, being added to each Fourier mode in the initial condition.

²This would have been exact if the summation had extended for all $j \in [1, N/2]$.

In Fig. 10 we plot the growth rate of the “noise floor” versus L . The theoretical values are inferred from the spectral radius of $\Phi(L)$, which was found by the above analysis, via the relation (see (45a)):

$$\text{growth rate} = (\ln \rho(\Phi(L)))/L. \quad (46)$$

The agreement between our analysis and direct numerics is seen to be quite good.

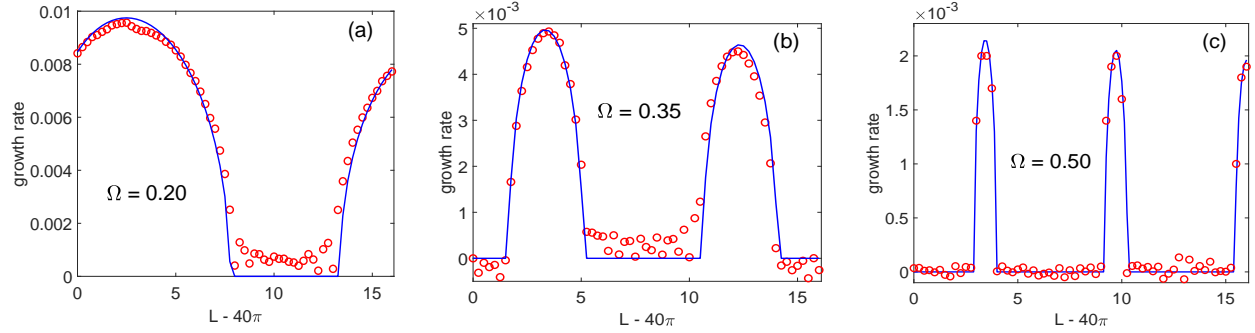


Figure 10: Growth rate of the “noise floor” as the function of length L of the computational domain for the same three values of Ω as in Fig. 7. Note different vertical scales in the three panels. Solid lines correspond to the analytical solution of (44), (46). Circles are the result of SSM simulation, where we measured the amplitude of the Fourier harmonic at $k = k_{\max}/2$ and followed the procedure described at the end of Section 5. The simulation times for panels (b) and (c) are the same as those in Figs. 6(b,c) and 7(b,c): $t = 1500$ and $t = 5000$. For panel (a), the simulation time is $t = 1000$. This larger time than in Figs. 6(a) and 7(a) had to be used to decrease the effect of the transient behavior (see Figs. 9(b,c)) on the computed growth rate (see text). Moreover, since for $\Omega = 0.2$, the NI at $k \approx \pm k_{\max}$ is so strong that it would destroy the numerical solution at $t = 1000$ (see Fig. 7(a)), we had to filter out harmonics near the edges of the computational spectral domain.

The numerical solution of system (44) leaves it unclear why $\rho(\Phi(L))$ depends on L . Moreover, such a dependence may even seem counter-intuitive given that the amplitude of the perturbation (34) changes only in the vicinity of the soliton (which does not depend on L) and remains intact in the rest of the computational domain. In Appendix D we show that while $\|\Phi(L)\|$ does not depend on L , $\rho(\Phi(L))$ varies with L periodically, the period being $2\pi/(2\Omega)$, which is confirmed by Fig. 10. Note that these different dependences of $\|\Phi(L)\|$ and $\rho(\Phi(L))$ on L are consistent with the well-known (see, e.g., [35]) result:

$$\rho(\Phi(L)) \leq \|\Phi(L)\| = \sigma_{\max}(\Phi(L)), \quad (47)$$

where σ_{\max} denotes the largest singular value.

To conclude this section, we note that while the “noise floor” NI decreases when Ω increases, it is still present even for a non-fragile soliton with $\Omega = 0.75$. In that case, Eqs. (44) and (46) predict that the NI growth rate peaks to about $2.9 \cdot 10^{-4}$, i.e., slightly lower than the spectral edge NI, near $L = 40\pi + 3.1$. Simulations by the SSM support this analytical result. Moreover, they reveal a feature of this NI that was not observed for $\Omega \leq 0.5$. Namely, for certain L values, only part of

the “noise floor” would become unstable. Analysis of this phenomenon would be more complicated than that based on the k -independent ansatz (39) and therefore is not considered here.

7 Generalizations

Here we will show that the two types of NI considered in Sections 5 and 6 occur in more general situations than in simulations of a single Gross–Neveu soliton. Thus, these types of NI appear to be engendered not by a specific model, its solution, or even the numerical method, but by a combination of various factors. Namely, we will first show that the same phenomena occur for more general solutions of the same model. Second, we will show that one of them occurs for the soliton of a different, well-known model in the relativistic field theory. Third, we will explain why, and show that, the same types of NI occur in other popular numerical methods applied to the Gross–Neveu model. Finally, we will show that by changing the boundary conditions of the numerical method, one can strongly diminish both types of NI.

7.1 More general solutions of the Gross–Neveu model

In Fig. 11 we show the result of simulation of two colliding solitons (6). The parameters of the solitons are: $\Omega_1 = 0.25$, $V_1 = 0$, $(x_0)_1 = 0$; $\Omega_2 = 0.15$, $V_2 = 0.1$, $(x_0)_2 = -8\pi$. Other simulation parameters are: $L = 160\pi$, $N = 2^{14}$, $\Delta t = \Delta x/5$, where the computational domain was chosen to be larger than that in the rest of this paper to minimize the effect of radiation re-entering the domain and possibly corrupting the solution. The NI at the edges of the spectral domain is clearly visible. Moreover, one can see that the spectral support of unstable modes greatly expands between $t = 175$ and $t = 200$, which is when the moving soliton comes in close proximity with the standing one

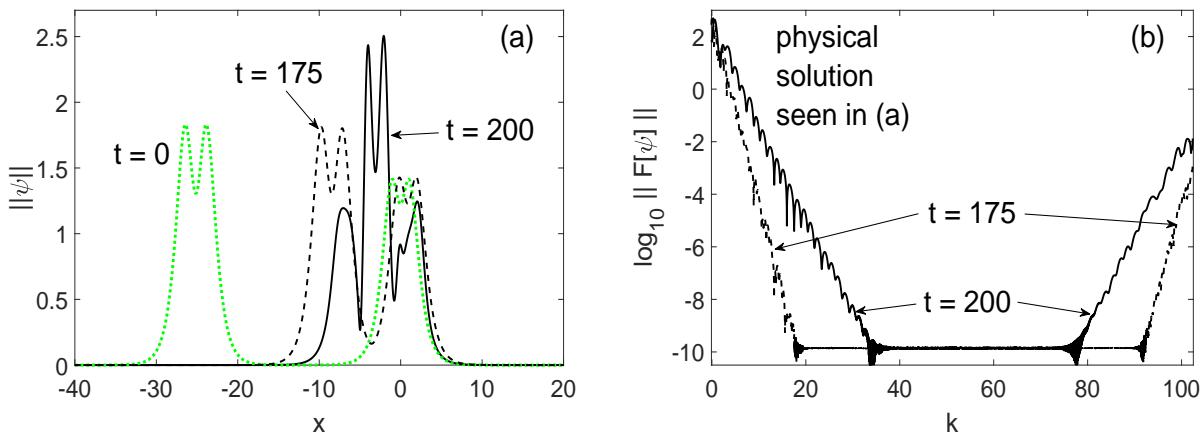


Figure 11: Colliding solitons described in Section 7.1. Panel (a): Dotted (green), dashed, and solid lines correspond to the solution at $t = 0$, 175, and 200. Only part of the computational domain is shown for better visibility. Panel (b): Spectra (for $k \geq 0$) of the numerical solution at $t = 175$ (dashed) and $t = 200$ (solid).

We also considered the evolution of an initial pulse both of whose components are 20% greater

than those of the standing soliton (5) with $\Omega = 0.2$. The NI at the edges of the computational domain destroys the resulting near-soliton solution by $t \gtrsim 300$. It should be noted that some other combinations of the components of the initial pulse, — e.g., where one is 20% greater and the other is 20% smaller than those of the soliton, — do *not* lead to a strong NI. This occurs because such an initial pulse evolves towards a soliton with a greater value of Ω , for which the NI is considerably weaker.

7.2 Numerical instability for the massive Thirring soliton

The massive Thirring model in laboratory coordinates:

$$u_t + u_x = i(v + u|v|^2), \quad v_t - v_x = i(u + v|u|^2), \quad (48)$$

has the one-soliton solution [33, 36, 37] which, for zero velocity, can be written as:

$$U_{\text{sol}} = \frac{\sin Q \exp[-it \cos Q]}{\cosh(x \sin Q - iQ/2)}, \quad V_{\text{sol}} = \frac{-\sin Q \exp[-it \cos Q]}{\cosh(x \sin Q + iQ/2)}, \quad Q \in [0, \pi]. \quad (49)$$

It may be noted that the Gross–Neveu and massive Thirring models both belong to the more general class of fermionic (nonlinear Dirac) field-theoretic models, corresponding to the cases of scalar–scalar and vector–vector interactions, respectively [33]. The massive Thirring model is integrable by the Inverse Scattering Transform [38, 39], a consequence of which is that the soliton solution (49) is physically stable [40]. Incidentally, a model similar to (48) occurs in a different field — that of nonlinear light propagation in optical fibers with a periodic refractive index [41]. However, its soliton (known as the Bragg, or gap, soliton) is physically unstable in a certain range of its parameters [42]. Therefore, we chose to consider only the stable soliton (49) of model (48) to avoid any issue of possible coexistence of physical and numerical instabilities.

To apply the SSM to (48), one first solves the linear part of those equations in the Fourier domain:

$$\begin{pmatrix} \hat{u} \\ \hat{v} \end{pmatrix}_{\text{lin}} = \frac{1}{1 + \delta^2} \begin{pmatrix} e^{i\gamma\Delta t} + \delta^2 e^{-i\gamma\Delta t} & \delta (e^{i\gamma\Delta t} - e^{-i\gamma\Delta t}) \\ \delta (e^{i\gamma\Delta t} - e^{-i\gamma\Delta t}) & \delta^2 e^{i\gamma\Delta t} + e^{-i\gamma\Delta t} \end{pmatrix} \begin{pmatrix} \hat{u} \\ \hat{v} \end{pmatrix}_n, \quad (50a)$$

where $\gamma = \sqrt{k^2 + 1}$, $\delta = k + \gamma$. Then the nonlinear substep is:

$$\begin{pmatrix} \hat{u} \\ \hat{v} \end{pmatrix}_{n+1} = \begin{pmatrix} u_{\text{lin}} \exp[i|v_{\text{lin}}|^2 \Delta t] \\ v_{\text{lin}} \exp[i|u_{\text{lin}}|^2 \Delta t] \end{pmatrix}. \quad (50b)$$

Using the SSM (50) to simulate (48) with the initial condition consisting of the soliton (49) with $Q = 0.35\pi$ and white noise of magnitude on the order of 10^{-12} , we have observed the numerically unstable modes at the edges of the spectrum grew by 7 orders of magnitude in $t = 1000$. The simulation parameters were: $L = 40\pi$, $N = 2^{12}$, and $\Delta t = \Delta x/5$. The spectrum of the numerical solution looks qualitatively similar to that shown in Fig. 3(a) and therefore is not shown here.

For greater Q , this NI developed even faster.³ Conversely, for smaller Q , we found that this NI decreases. For example, for $Q = 0.30\pi$ we found that the unstable modes at the spectral edges grow at most by two orders of magnitude when we performed this simulation for a variety of values of L .

We were unable to observe the “noise floor” NI for the Massive Thirring soliton in our numerics for any values of Q and L and initially were surprised. However, an analysis similar to that presented in Section 6 revealed that for this model, this type of NI does not occur. Below we present a summary of this analysis. Although it is possible to apply it directly to Eqs. (48), it is more convenient to cast those equation in a form with the l.h.s. identical to that of the Gross–Neveu model (2) so as to follow the analysis of Section 6 as closely as possible. To that end, defining

$$\psi_1 = (u + v)/\sqrt{2}, \quad \psi_2 = (u - v)/\sqrt{2}, \quad (51)$$

we transform (48) into

$$\psi_{1,t} + \psi_{2,x} = \frac{i}{2} (\psi_1 |\psi_1|^2 - \psi_1^* \psi_2^2) + i\psi_1, \quad \psi_{2,t} + \psi_{1,x} = \frac{i}{2} (\psi_2 |\psi_2|^2 - \psi_2^* \psi_1^2) - i\psi_2, \quad (52)$$

Linearizing (52), we obtain equations of the form (8a) with Ω on the l.h.s. being replaced by $\cos Q$ and with:

$$P_0 = \frac{1}{2} (|\Psi_1|^2 + |\Psi_2|^2), \quad P_1 \equiv 0, \quad Q_0 \equiv 0, \quad Q_1 \equiv 0, \quad (53a)$$

$$P_2 = -\text{Im} (\Psi_1 \Psi_2^*), \quad P_3 = \frac{1}{2} (|\Psi_1|^2 - |\Psi_2|^2) + 1, \quad Q_2 \equiv 0, \quad Q_3 = \frac{1}{2} (\Psi_1^2 - \Psi_2^2), \quad (53b)$$

where $\Psi_{1,2}$ are the exact one-soliton solutions obtained from (49) and (51). In deriving $P_1 \equiv 0$, we used the specific form (49) of the soliton. The information about the possible growth of the “noise floor” perturbation is found from Eqs. (42a), where the matrix on the r.h.s. is now:

$$\mathbf{R}_{(\pm)} = i\sigma_3 \left(\cos Q \sigma_0 + \begin{pmatrix} P_0(t) & 0 \\ 0 & P_0(t) \end{pmatrix} \right), \quad (54)$$

where we have used that P_0 is a real-valued and even function. The key point to note is that due to the absence of off-diagonal terms in (54), the evolution of the perturbation \mathbf{c} is unitary, and hence there is no “noise floor” NI in this case.

7.3 Numerical instability of other methods applied to Gross–Neveu soliton

In our analysis of the NI in Sections 5 and 6 there was nothing that would explicitly refer to the SSM as opposed to any other numerical method. Indeed, all we did was obtain a differential (in time) equation for the error in the limit $\Delta t \rightarrow 0$. There was, however, an *implicit* assumption: that the numerical scheme does not change the linear dispersion relation (11) (for $|k| \gg 1$). Therefore, we expect that similar NI should occur for any other numerical scheme that preserves the linear dispersion relation of models (2) and (48).

³ The limit $Q \rightarrow \pi$ for the massive Thirring soliton is known to have similarities with the limit $\Omega \rightarrow 0$ for the Gross–Neveu soliton.

One such family of schemes is the Exponential Time Differencing (ETD) and Integrating Factor methods (see, e.g., [43]). It should be noted that for the Gross–Neveu model, such methods were first proposed in [44] and have recently been considered in [18]. We implemented the ETD method based on the 4th-order explicit Runge–Kutta (RK) solver, referred to as ETD4RK in [43] and given by Eqs. (26)–(29) in that paper. For the implementation of the ETD methods, it is convenient to rewrite the simulated equation in a form where the matrix multiplying the spatial derivative terms is diagonal. For Eqs. (2) this is achieved via the transformation inverse to (51), upon which they take on the form:

$$u_t = -u_x + i(u|v|^2 + u^*v^2 - v), \quad v_t = v_x + i(v|u|^2 + v^*u^2 - u). \quad (55)$$

In simulating the Gross–Neveu equations in this form with the ETD4RK, we observed both types of NI — at the spectral edges and of the “noise floor”, — with their growth rates being practically the same (for the selected values of L that we tested) to those reported in Sections 5 and 6, as long as $\Delta t < \Delta x$ (see (12)).

The other method for which we tested the presence of NI in the Gross–Neveu model is the pseudo-spectral 4th-order RK method. To implement it, one solves Eqs. (55) (or (2)) by the classical RK method in time, with the spatial derivatives being computed by the direct and inverse Fourier transform (15). This method preserves the dispersion relation (11) *only* in the limit $k_{\max}\Delta t \equiv (\pi/\Delta x)\Delta t \ll 1$, where the 4th-degree polynomial in $k\Delta t$, which results from the 4th-order RK method, approximates $\exp[ik\Delta t]$ sufficiently closely for all wavenumbers. However, recall that we are interested in demonstrating the *unconditional* NI, which persists in the limit $\Delta t \rightarrow 0$. Therefore, at least for sufficiently small Δt , the NI in the pseudo-spectral method is expected to develop similarly to that in the SSM. We confirmed this to indeed be the case. For example, for $\Omega = 0.2$, the NI at the spectral edge was suppressed by the numerical diffusion of the pseudo-spectral method for $\Delta t = \Delta x/5$; however, for $\Delta t = \Delta x/10$, the numerical diffusion became weak enough to allow this NI to develop almost as fast as in the SSM. For $\Omega = 0.1$, even the relatively strong numerical diffusion was not able to prevent the NI at the spectral edge from destroying the numerical solution around $t = 200$. Also, the “noise floor” NI in the pseudo-spectral method was similar to that in the SSM for both $\Delta t = \Delta x/5$ and $\Delta t = \Delta x/10$.

7.4 Suppression of the numerical instability for the Gross–Neveu soliton

The previous subsection illustrated the fact that the appearance of NI in simulations of the Gross–Neveu soliton with sufficiently small Ω occurs not just for the Fourier SSM, but for a variety of numerical methods. In fact, NI for this problem was earlier reported in [29, 30], although no details about its nature were investigated in those studies. On the other hand, we showed in [32] that merely imposing *nonreflecting* boundary conditions (BC):

$$u(-L/2) = 0, \quad v(L/2) = 0, \quad (56)$$

which is done by using the numerical method of characteristics, allows the small- Ω soliton to survive over several thousands of time units. Imposing additional absorption at the boundaries was shown [32] to further increase soliton’s survival time, thus making it numerically stable even in ultra-long simulations, in accordance with the theoretical prediction of [31].

Let us mention in passing that nonreflecting BC (56) alone, i.e., without the additional absorber at the boundaries, do not entirely eliminate NI for sufficiently small Ω (e.g., for $\Omega = 0.1$). Indeed, as shown in [32], the key to suppress NI is to let any radiation *completely* leave the computational domain without being partially reflected inside it by the boundaries. (In the case of periodic BC, such a reflection is replaced by mere re-entrance of the radiation into the domain.) Nonreflecting BC (56) allow the radiation to completely leave the computational domain, without being reflected back (hence the name), *only* in the absence of terms other than u_x, v_x on the r.h.s. of (55). *With* the other terms, the amount of radiation reflected back into the domain is proportional to $1/k$. Hence higher harmonics are suppressed more than the lower ones; yet it is the lower harmonics that appear to be “responsible” for soliton’s “fragility” (see Section 2). This is why the additional absorber, that would equally absorb *all* harmonics, was needed in [32] to avert destruction of the soliton.

8 Conclusions and Discussion

In this work, we showed that the (Fourier) SSM, (10) or (14), for the Gross–Neveu model (2) may exhibit NI, and analytically studied three distinct mechanisms that can lead to it. Two of these mechanisms lead to *unconditional* NI, which, to our knowledge, have never been analyzed previously.

The first type of NI, analyzed in Section 4, *may* occur when the time step exceeds the “threshold” (12) set by the Courant–Friedrichs–Lewy condition. However, unlike in other schemes for hyperbolic equations, this high- k NI is observed *only* if the simulated solution of the model also exhibits low- k instability. In practice, such conditional NI (unlike that for the NLS!) is inconsequential for the outcome of the simulations. Indeed, if a low- k instability is present, it will destroy the solution long before this high- k NI will. On the other hand, if there is no (or too weak) low- k instability, then harmonics near the “resonance” wavenumber k_π will also be stable, even when the time step exceeds the “threshold” (12).

The NI of the second type, analyzed in Section 5, occurs near the edges of the computational spectrum. It is *unconditional*, i.e. persists for arbitrarily small Δt . This type of NI becomes stronger as Ω of the soliton decreases, i.e., as the soliton becomes more “fragile”. While the corresponding growth rate depends on the length L of the computational domain, this dependence diminishes as Ω decreases: see Figs. 7 and 8(b). There is no “simple” qualitative reason that would unambiguously explain the origin of this NI. Analysis of this NI required numerical solution of a relatively large eigenvalue problem, but this is still several orders of magnitude faster than direct numerical simulations, especially for non-fragile solitons.

The NI of the third type, analyzed in Section 6, occurs for Fourier harmonics of the “noise floor”. This NI is also unconditional, and it also becomes stronger as Ω of the soliton decreases. The growth rate is essentially periodic in L , but also decreases in inverse proportion to it (i.e., for a sufficiently large L , slowly). Unlike for the second type of NI, there *is* a qualitative explanation for the third one. Namely, it can occur as perturbations travelling in the opposite directions interact in the vicinity of the soliton via the “potential” created by it. This process can be amplified when the perturbations do so repeatedly, which is enabled by their staying in the computational domain due to periodic boundary conditions. Analysis of this NI requires numerical solution of only two coupled ordinary differential equations; see Eqs. (42) and (44). Remarkably, the same analysis was able to explain the *absence* of the “noise floor” NI in the massive Thirring model (Section 7.2).

In Section 7, we demonstrated that these two types of unconditional NI can occur in more general situations. First, they occur in multi-soliton solutions, as long as some of the constituent solitons have a sufficiently small Ω . Second, they can occur for other models that involve solitons in asymptotically dispersionless coupled-mode equations; an example is the massive Thirring soliton. Third, they can occur for methods other than the SSM.

Based on these generalizations, we propose that there may be only two essential conditions that need to be met for these unconditional NIs to be observed. The first is that the simulated soliton’s parameters must be in a certain range (e.g., a sufficiently small Ω for the Gross–Neveu soliton or a sufficiently large Q for the massive Thirring soliton). Although these NIs were found even for Gross–Neveu solitons with Ω as large as 0.75,⁴ their growth rates were too small to be observed in any but the ultra-long simulations.

The second essential condition for observing these NIs is the boundary conditions that permit a substantial part of the radiation to re-enter the computational domain. The simplest such BC are periodic; they are automatically imposed when the numerical method involves the discrete Fourier transform. However, there are indications in [30] that other BC, such as homogeneous Dirichlet, may also lead to similar NIs. As we showed in [32] and stressed in Section 7.4, only a combination of nonreflecting BC and an additional absorber (or a more sophisticated technique [45]) could suppress NI for solitons with arbitrarily small Ω .

We now relate our results with those of [29, 30], where numerical instabilities of the Gross–Neveu soliton were reported. The authors of [29] used a 4th-order non-Fourier SSM, where the linear substep was computed by the method of characteristics, subject to nonreflecting BC (56). The evidence of high- k NI is reported there in the captions to Figs. 5 and 6. This may be surprising given that we argued in Section 7.4 that the nonreflecting BC tend to suppress high- k NI (and so a low- k NI would be observed before any high- k could be seen). A detailed analysis of this conundrum would require a separate study and is clearly outside the scope of this one. Below we present only a plausible resolution, which consists of two ingredients. First, it should be noted that the 4th-order method of [29] required a relation $\Delta t = 12\Delta x$. Thus, the stability “threshold” (12) was exceeded

⁴ and we have no reason to think that they would not occur for even greater Ω

significantly. Had the method been 2nd-order, as here, this would not have caused a high- k NI to destroy the soliton. However, it was shown in [16] that the equation satisfied by a high- k numerical error in a 4th-order method is different from that for the 2nd-order one. This fact makes it possible for the modes near the “resonant” wavenumbers $k_{n\pi}$, $n = 1, \dots, 12$ to become unstable regardless of any low- k NI. In fact, the numerical solution reported in [29] for the soliton with $\Omega = 0.1$ at $t = 100$, was provided to this author in a private communication by the first co-author of [29], and it *confirmed* the above hypothesis about an NI developing near the “resonant” wavenumbers $k_{n\pi}$, $n = 1, \dots, 12$.

The authors of [30] employed three methods to simulate the dynamics of the soliton. Their best-performing method is, in fact, the pseudo-spectral method considered in Section 7.3. As we showed there, this method is subject to the same NIs as the SSM. Moreover, the NIs would become more pronounced as one decreases $\Delta t/\Delta x$, because it is then suppressed less by numerical diffusion. In [30], the authors conspicuously stated that the NIs should go away as $L \rightarrow \infty$ and $\Delta x \rightarrow 0$. However, our analysis indicates that both of these statements are incorrect. Namely, Figs. 7(a) and 8(b) show that the growth rate of the spectral edge NI for sufficiently small Ω persists almost unchanged from $L = 40\pi$ to $L = 1600\pi \approx 5,000$, which is more than 30 times the largest length considered in [30]. We also verified that for the same length as used in most of the simulations in this work, $L = 40\pi$, and for $N = 2^{17}$ ($\Delta x \approx 10^{-3}$, i.e. 32 times smaller than in the rest of the work) the growth rate of the $\Omega = 0.2$ soliton was the same as for $N = 2^{12}$ ($\Delta x \approx 0.03$). Thus, the spectral edge NI is not perceptibly affected by either the $L \rightarrow \infty$ or $\Delta x \rightarrow 0$ limits. The “noise floor” NI is not affected by the $\Delta x \rightarrow 0$ limit, but its growth rate does indeed vanish as $L \rightarrow \infty$ since it scales as $1/L$.

Finally, we note that results of our study should alert researchers who numerically study new models similar to the Gross–Neveu model (see, e.g., [46, 47]) about possible NI that may occur in simulations of those models. Our analysis may also serve as a prototype for that of the Zakharov equations, describing interaction of short and long waves [48]. They consist of an NLS coupled to the hyperbolic nonlinear wave equation. The dispersion relation of the latter equation, which for high wavenumbers coincides with (11), may potentially enable an NI similar to those considered in this work. In fact, an indication of a possible NI in simulations of the Zakharov equations by an SSM is reported in Fig. 10 of [11].

Acknowledgments

This work was supported in part by the NSF grant DMS-1217006. The author acknowledges a useful conversation with J. Yang and thanks S. Shao for providing the numerical results mentioned three paragraphs above.

Appendix A: Code of 2nd-order SSM for Gross–Neveu soliton

```

1 clear all;
2 % — Simulation parameters:
3 L = 40*pi; N = 2^12; dx = L/N; x = [ -L/2 :dx: L/2-dx ];
4 dk = 2*pi/L; k = [ 0 : N/2-1 -N/2 : -1 ]*dk;
5 dt = dx/2; tmax = 1500; tplot = 50;
6 % — Initial conditions:
7 Omega = 0.35; beta = sqrt( 1 - Omega^2 ); mu = (1 - Omega)/(1 + Omega);
8 u0 = sqrt(2*(1 - Omega))./( (1 - mu*tanh(beta*x)).^2).*cosh(beta*x);
9 v0 = 1i*u0.*sqrt(mu).*tanh(beta*x);
10 u = u0 + 10^(-12)*randn(size(x)); v = v0 + 10^(-12)*randn(size(x));
11 % — Auxiliary parameters to be used at each step in the loop:
12 idt = 1i*dt; ckdt = cos(k*dt); mi_skdt = -1i*sin(k*dt);
13 ckdto2 = cos(k*dt/2); mi_skdto2 = -1i*sin(k*dt/2);
14 % — Main calculation:
15 for mn = 1 : round(tmax/dt)
16     fftu = fft(u); fftv = fft(v);
17     if mn == 1
18         u = ifft( ckdto2.*fftu + mi_skdto2.*fftv );
19         v = ifft( ckdto2.*fftv + mi_skdto2.*fftu );
20     else
21         u = ifft( ckdt.*fftu + mi_skdt.*fftv );
22         v = ifft( ckdt.*fftv + mi_skdt.*fftu );
23     end
24     expaux = exp( idt*( abs(u).^2-abs(v).^2 - 1) );
25     u = u.*expaux; v = v./expaux;
26     if mn == round(tmax/dt)
27         u = ifft( ckdto2.*fftu + mi_skdto2.*fftv );
28         v = ifft( ckdto2.*fftv + mi_skdto2.*fftu );
29     end
30     % — Plot the results:
31     if rem(mn, round(tplot/dt)) == 0
32         figure(123);
33         subplot(211); plot(x, abs(u), 'b', x, abs(v), 'r');
34         xlabel('x'); ylabel('{|u|, |v|}');
35         subplot(212); plot(k, log10(abs(fftu)), 'b', k, log10(abs(fftv)), 'r
36         ');
37         xlabel('k, wavenumber'); ylabel('log_{10}(|F[u, v](k)|)');
38         title(['t=', num2str(dt*mn)], 'fontsize', 13); pause(0.3)
39     end
40 end

```

Appendix B: Weak fragility of solitons with $\Omega > 0.6$

Simulations reported in Section 3.1 illustrated our general observation that if the soliton is fragile, then exponentially growing modes will appear around $k_{n\pi}$ -peaks whenever $\Delta t > \Delta x$. One can conjecture that the converse statement may also be true, namely: If one detects such modes around

$k_{n\pi}$ -peaks, then the soliton must be (weakly) fragile, even though it has not yet exhibited any fragile behavior for the same simulation time. In other words, can a high- k instability signal the occurrence of a low- k one?

In Fig. 12 we demonstrate that this is indeed the case. In panel (a) we show a close-up on the vicinity of the k_π -peak for the $\Omega = 0.75$ -soliton at $t = 15,000$, where exponentially growing “spikes” near the wider k_π -peak are clearly discernible. For the same t , there is no sign of fragile behavior of this numerical solution in either the Fourier domain (panel (b)) or x -domain (not shown). However, at a much greater time, a small “spike” becomes visible within the soliton’s own spectrum (around $k = 5$); see Fig. 12(b). Finally, Fig. 12(c) shows that one can detect the exponentially growing modes around the k_π -peaks much earlier than similarly growing modes around the soliton.

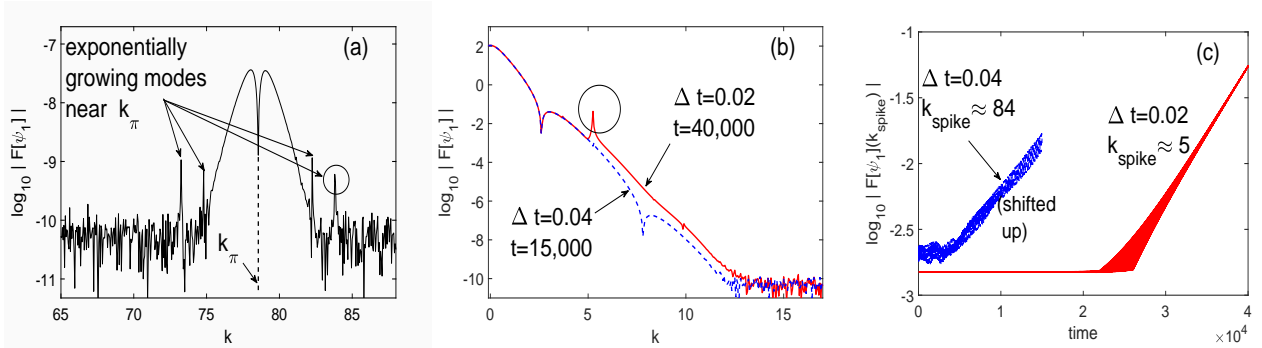


Figure 12: Ultra-long-time simulations of $\Omega = 0.75$ -soliton (non-fragile). Simulation parameters are: $L = 40\pi$, $N = 2^{12}$ ($\Delta x = \Delta t_{\text{thresh}} \approx 0.031$). Results for the ψ_2 -component are similar to those for the ψ_1 -component and hence are not shown. (a) Close-up on the vicinity of the k_π -peak for $\Delta t = 0.04 \approx 1.3\Delta x$ and $t = 15,000$. (b) Solitonic part of the spectrum of the numerical solution obtained at different times and with different Δt . The lines are indistinguishable for $k < 5$. (c) Evolution of the amplitudes of the “spikes” circled in panels (a) and (b). The left curve is shifted up by 7.2 units for better visibility.

Two clarifications regarding the above result are in order. First, the reason that exponentially growing modes are observed sooner around the k_π -peak is that the “noise floor”, from which these modes arise, is several orders of magnitude closer to the k_π -peak than to the soliton’s spectral maximum. Thus, it takes less time for such modes to become visible relative to the k_π -peak than relative to the soliton. Second, the reason why the emergence of the exponential instability is significantly delayed from the start of the simulations (see Fig. 12(c)) was explained in [49]. It is related to the fact that both (i) the overlap of the actual unstable mode with any one Fourier harmonic and (ii) the instability growth rate, are small.

Appendix C: Reduced form of Eqs. (30), and matrix blocks in (33c)

Substitution of (31) and (32) into Eqs. (30) and taking complex conjugate of two of the four equations yields the following system:

$$\hat{a}_{(+),t} = \tag{C.1a}$$

$$i \left(\Omega - \delta k^{(<0)} \right) \hat{a}_{(+)} + i \mathcal{F} \left[\left[P_0 a_{(+)} + (iP_2 + P_3)b_{(-)} + Q_3 a_{(-)}^* + (Q_0 + Q_1)b_{(+)}^* \right]^{(<0)} \right],$$

$$\widehat{b}_{(-),t} = \quad (C.1b)$$

$$i \left(\Omega + \delta k^{(\geq 0)} \right) \widehat{b}_{(-)} + i \mathcal{F} \left[\left[(-iP_2 + P_3)a_{(+)} + P_0 b_{(-)} + (Q_0 - Q_1)a_{(-)}^* + Q_3 b_{(+)}^* \right]^{(\geq 0)} \right].$$

$$\widehat{a}_{(-),t}^* = \quad (C.1c)$$

$$-i \left(\Omega + \delta k^{(< 0)} \right) \widehat{a}_{(-)}^* - i \left(\mathcal{F} \left[\left[(Q_3 a_{(+)}^* + (Q_0 - Q_1)b_{(-)}^* + P_0 a_{(-)} + (-iP_2 + P_3)b_{(+)} \right]^{(< 0)} \right] \right)^*,$$

$$\widehat{b}_{(+),t}^* = \quad (C.1d)$$

$$-i \left(\Omega - \delta k^{(\geq 0)} \right) \widehat{b}_{(+)}^* - i \left(\mathcal{F} \left[\left[(Q_0 + Q_1)a_{(+)}^* + Q_3 b_{(-)}^* + (iP_2 + P_3)a_{(-)} + P_0 b_{(+)} \right]^{(\geq 0)} \right] \right)^*.$$

Here we have also used that $P_1 = Q_2 = 0$ from (8).

The $M \times M$ matrix blocks \mathbb{C}_{1m} , $m = 1, \dots, 4$, in (33c) are obtained from the respective four convolution-like terms in (C.1a). Similarly, the other blocks are obtained from the respective terms in (C.1b)–(C.1d). Here we will present a derivation of \mathbb{C}_{11} and \mathbb{C}_{12} and will state the results for the other \mathbb{C}_{jm} , which are derived analogously.

To obtain the form of \mathbb{C}_{11} , we substitute the first relation from (27) into the first \mathcal{F} -term in (C.1a) and use the definitions of discrete Fourier transform and its inverse (15) to obtain the following expression for the harmonic with wavenumber $k_{-j} = -j\Delta k$, where $1 \leq j \leq M$:

$$\begin{aligned} \mathcal{F} [P_0 a_{(+)}]_{-j} &= \sum_{m=-N/2}^{N/2-1} e^{-ik_{-j}x_m} \frac{1}{N} \sum_{n=-N/2}^{N/2-1} \widehat{P}_{0n} e^{ik_n x_m} \frac{1}{N} \sum_{l=1}^M \widehat{a}_{(+),l} e^{-ik_l x_m} \quad (C.2) \\ &= \frac{1}{N^2} \sum_{n=-N/2}^{N/2-1} \widehat{P}_{0n} \sum_{l=1}^M \widehat{a}_{(+),l} \delta_{n, l-j} = \frac{1}{N} \sum_{l=1}^M \widehat{P}_{0, l-j} \widehat{a}_{(+),l}; \end{aligned}$$

in the last line, δ is the Kroneker symbol. Therefore,

$$\mathbb{C}_{11} = \begin{pmatrix} \widehat{P}_{00} & \widehat{P}_{01} & \cdots & \widehat{P}_{0, M-1} \\ \widehat{P}_{0, -1} & \widehat{P}_{00} & \cdots & \widehat{P}_{0, M-2} \\ \vdots & \vdots & \ddots & \vdots \\ \widehat{P}_{0, -(M-1)} & \widehat{P}_{0, -(M-2)} & \cdots & \widehat{P}_{00} \end{pmatrix}. \quad (C.3a)$$

This is a Toeplitz matrix, and half of the entries in (33c) will also be Toeplitz. Therefore, we introduce a notation:

$$\mathbb{C}_{11} \equiv \mathcal{T} [P_0, -(M-1), M-1], \quad (C.3b)$$

where: \mathcal{T} stands for a Toeplitz matrix, the first argument indicates the function whose harmonics make up the entries of the matrix, and the third and fourth entries indicate the harmonic's indices of the lower-left and upper-right entries of the matrix, respectively.

Similarly, and denoting $iP_2 + P_3 \equiv P_{i23}$ for brevity, one has:

$$\begin{aligned} \mathcal{F} [P_{i23} b_{(-)}]_{-j} &= \sum_{m=-N/2}^{N/2-1} e^{-ik_{-j}x_m} \frac{1}{N} \sum_{n=-N/2}^{N/2-1} \widehat{P}_{i23n} e^{ik_n x_m} \frac{1}{N} e^{-i\Delta k x_m} \sum_{l=1}^M \widehat{b}_{(-),l} e^{ik_l x_m} \quad (C.4) \\ &= \frac{1}{N} \sum_{l=1}^M \widehat{P}_{i23, 1-l-j} \widehat{b}_{(-),l}; \end{aligned}$$

whence

$$\mathbb{C}_{12} = \begin{pmatrix} \widehat{P}_{i23-1} & \widehat{P}_{i23-2} & \cdots & \widehat{P}_{i23-M} \\ \widehat{P}_{i23-2} & \widehat{P}_{i23-3} & \cdots & \widehat{P}_{i23-M-1} \\ \ddots & \ddots & \ddots & \ddots \\ \widehat{P}_{i23-M} & \widehat{P}_{i23-M-1} & \cdots & \widehat{P}_{i23-2M+1} \end{pmatrix}. \quad (\text{C.5a})$$

This is a Hankel (i.e. an ‘‘upside-down’’ Toeplitz) matrix, and the remaining half of the entries in (33c) are also Hankel. Therefore, we introduce a notation:

$$\mathbb{C}_{12} \equiv \mathcal{H}[iP_2 + P_3, -1, -2M + 1], \quad (\text{C.5b})$$

where, similarly to (C.3b): \mathcal{H} stands for a Hankel matrix, the first argument indicates the function whose harmonics make up the entries of the matrix, and the third and fourth entries indicate the harmonic’s indices of the upper-left and lower-right entries of the matrix, respectively.

Similarly, one has:

$$\mathbb{C}_{13} = \mathcal{H}[Q_3, -2, -2M], \quad \mathbb{C}_{14} = \mathcal{T}[Q_0 + Q_1, -M, M - 2]; \quad (\text{C.6a})$$

$$\mathbb{C}_{21} = \mathcal{H}[-iP_2 + P_3, 1, 2M - 1], \quad \mathbb{C}_{22} = \mathcal{T}[P_0, M - 1, -(M - 1)], \quad (\text{C.6b})$$

$$\mathbb{C}_{23} = \mathcal{T}[Q_0 - Q_1, M - 2, -M], \quad \mathbb{C}_{24} = \mathcal{H}[Q_3, 0, 2M - 2];$$

$$\mathbb{C}_{31} = -\mathcal{H}[Q_3^*, -2, -2M], \quad \mathbb{C}_{32} = -\mathcal{T}[(Q_0 - Q_1)^*, -M, M - 2], \quad (\text{C.6c})$$

$$\mathbb{C}_{33} = -\mathcal{T}[P_0^*, -(M - 1), M - 1], \quad \mathbb{C}_{34} = -\mathcal{H}[(-iP_2 + P_3)^*, -1, -2M + 1];$$

$$\mathbb{C}_{41} = -\mathcal{T}[(Q_0 + Q_1)^*, M - 2, -M], \quad \mathbb{C}_{42} = -\mathcal{H}[Q_3^*, 0, 2M - 2], \quad (\text{C.6d})$$

$$\mathbb{C}_{43} = -\mathcal{H}[(iP_2 + P_3)^*, 1, 2M - 1], \quad \mathbb{C}_{44} = -\mathcal{T}[P_0^*, M - 1, -(M - 1)].$$

These matrix blocks can also be easily coded. For example, if `dftP0` and `dftPi23` denote the discrete Fourier spectra (15) with harmonics limited to $l \in [-2M, 2M]$ of P_0 and $(iP_2 + P_3)$, then the respective matrix blocks (C.3) and (C.5) can be programmed in Matlab as:

```
for j = 1 : M
    C_11(j, :) = dftP0(2*M+1 - (j-1) : 2*M+1 - (j-1) + (M-1));
    C_12(j, :) = dftPi23(2*M - (j-1) :-1: 2*M - (j-1) - (M-1));
end
```

Appendix D: Explanation of why and how the spectral range of $\Phi(L)$ depends on L

For the purpose of this explanation, it will suffice to replace the soliton with a box-like profile as follows. Since $\Psi_1(x)$ has a bell-like shape, we replace it by some constant for $x \in [-L_{\text{sol}}/2, L_{\text{sol}}/2]$. On the other hand, $i\Psi_2(x)$ changes sign at $x = 0$ (see Fig. 1), and therefore it needs to be replaced by a piecewise-constant profile on the same interval. Thus, we approximate:

$$\Psi_1(x) = \begin{cases} A, & x \in [-L_{\text{sol}}/2, L_{\text{sol}}/2] \\ 0, & |x| > L_{\text{sol}}/2 \end{cases}, \quad \Psi_2(x) = \begin{cases} \pm iB, & x \in [0, \pm L_{\text{sol}}/2] \\ 0, & |x| > L_{\text{sol}}/2 \end{cases}, \quad (\text{D.1a})$$

for some $A, B, L_{\text{sol}} > 0$, with $L_{\text{sol}} \ll L$. Then the t -dependent matrix on the r.h.s. of (44) is replaced with:

$$\begin{pmatrix} \Psi_1^2 - \Psi_2^2 & (\Psi_1 + \Psi_2)^2 \\ (\Psi_1 - \Psi_2)^2 & \Psi_1^2 - \Psi_2^2 \end{pmatrix} \equiv \begin{pmatrix} C & C e^{\pm i\phi} \\ C e^{\mp i\phi} & C \end{pmatrix}, \quad x \in [0, \pm L_{\text{sol}}/2] \quad (\text{D.1b})$$

and the zero matrix outside $[-L_{\text{sol}}/2, L_{\text{sol}}/2]$, where $C = A^2 + B^2$ and $\phi = 2 \arctan(B/A)$.

Using the replacement (D.1b), we can now calculate $\Phi(L)$ in (45) as

$$\Phi(L) \equiv \Phi_{L_{\text{sol}}} \Phi_{\text{free}}, \quad \Phi_{L_{\text{sol}}} = \begin{pmatrix} \Phi_{11} & \Phi_{12} \\ -\Phi_{12} & \Phi_{11}^* \end{pmatrix}, \quad \Phi_{\text{free}} = e^{i\Omega(L-L_{\text{sol}})\sigma_3} \quad (\text{D.2})$$

where the last matrix is obtained by solving the soliton-free part of (44) on an interval $t \in (L_{\text{sol}}/2, L - L_{\text{sol}}/2)$. The entries of $\Phi_{L_{\text{sol}}}$ depend on A, B , and L_{sol} in a complicated way, but their explicit form is not needed for our purpose; we will only require the result, found by a tedious calculation, that $\Phi_{12} \in i\mathbb{R}$. The eigenvalues λ of $\Phi(L)$ in (D.2) are found from the quadratic equation:

$$\lambda^2 - 2|\Phi_{11}| \cos[\Omega(L - L_{\text{sol}}) + \arg \Phi_{11}] \cdot \lambda + (|\Phi_{11}|^2 - |\Phi_{12}|^2) = 0. \quad (\text{D.3})$$

Since $\rho(\Phi(L)) = |\lambda|$, one can see that it varies with L periodically, with the period being $2\pi/(2\Omega)$. Moreover, as stated in (47),

$$\|\Phi(L)\| = \rho\left(\Phi(L) \Phi^\dagger(L)\right)^{1/2} = \rho\left(\Phi_{L_{\text{sol}}} \Phi_{L_{\text{sol}}}^\dagger\right)^{1/2} = |\Phi_{11}| + |\Phi_{12}|, \quad (\text{D.4})$$

where \dagger denotes Hermitian conjugation, and the last equation is found via a somewhat tedious but straightforward calculation. This result means that even when the ‘‘noise floor’’ does not grow *on average* over time, the amplitude of the ‘‘noise floor’’ harmonics can still increase by the factor $\|\Phi(L)\|$ over a time $t = L$; however, it will decrease in one or more of subsequent time intervals of the same length (see Figs. 10(b,c)).

References

- [1] G. Strang, On the construction and comparison of difference schemes, *SIAM J. Numer. Anal.* 5 (1968) 506–517.
- [2] M. Suzuki, Fractal decomposition of exponential operators with applications to many-body theories and Monte Carlo simulations, *Phys. Lett. A* 146 (1990) 319–323.
- [3] H. Yoshida, Construction of higher order symplectic integrators, *Phys. Lett. A* 150 (1990) 262–268.
- [4] M. Glassner, D. Yevick, B. Hermansson, High-order generalized propagation techniques, *J. Opt. Soc. Am. B* 8 (1991) 413–415.
- [5] A.D. Bandrauk, H. Shen, Exponential split operator methods for solving coupled time-dependent Schrödinger equations, *J. Chem. Phys.* 99 (1993) 1185–1193.

- [6] R.H. Hardin, F.D. Tappert, Applications of the split-step Fourier method to the numerical solution of nonlinear and variable coefficient wave equations, *SIAM Review (Chronicle)* 15 (1973) 423.
- [7] T. Taha, M. Ablowitz, Analytical and numerical aspects of certain nonlinear evolution equations. II. Numerical, Nonlinear Schrödinger equation, *J. Comput. Phys.* 55 (1984) 203–230.
- [8] W. Bao, H. Wang, An efficient and spectrally accurate numerical method for computing dynamics of rotating Bose–Einstein condensates, *J. Comput. Phys.* 217 (2006) 612–626.
- [9] C.Z. Cheng, G. Knorr, The integration of the Vlasov equation in configuration space, *J. Comput. Phys.* 22 (1976) 330–351.
- [10] J. de Frutos, J.M. Sanz-Serna, Split-step spectral schemes for nonlinear Dirac systems, *J. Comput. Phys.* 83 (1989) 407–423.
- [11] W. Bao, F. Sun, G.W. Wei, Numerical methods for the generalized Zakharov system, *J. Comput. Phys.* 190 (2003) 201–228.
- [12] S. Jin, P.A. Markowich, C. Zheng, Numerical simulation of a generalized Zakharov system, *J. Comput. Phys.* 201 (2004) 376–395.
- [13] J.A.C. Weideman, B.M. Herbst, Split-step methods for the solution of the nonlinear Schrödinger equation, *SIAM J. Numer. Anal.* 23 (1986) 485–507.
- [14] L. Gauckler, C. Lubich, Splitting integrators for nonlinear Schrödinger equations over long times, *Found. Comput. Math.* 10 (2010) 275–302.
- [15] E. Faou, B. Grébert, E. Paturel, Birkhoff normal form for splitting methods applied to semi-linear Hamiltonian PDEs. Part I. Finite-dimensional discretization, *Numer. Math.* 114 (2010) 429–458.
- [16] T.I. Lakoba, Instability analysis of the split-step Fourier method on the background of a soliton of the nonlinear Schrödinger equation, *Numer. Methods Partial Differ. Equ.* 28 (2012) 641–669.
- [17] J. Xu, S. Shao, H. Tang, Numerical methods for nonlinear Dirac equation, *J. Comput. Phys.* 245 (2013) 131–149.
- [18] W. Bao, Y.Y. Cai, X.W. Xia, J. Yin, Error estimates of numerical methods for the nonlinear Dirac equation in the nonrelativistic limit regime, *Sci. China Math.* 59 (2016) 1461–1494.
- [19] S.-C. Li, X.-G. Li, F.-Y. Shi, Time-splitting methods with charge conservation for the nonlinear Dirac equation, *Numer. Methods Partial Differ. Equ.* 33 (2017) 1582–1602.
- [20] M. Lemou, F. Méhats, X. Zhao, Uniformly accurate numerical schemes for the nonlinear Dirac equation in the nonrelativistic limit regime, *Commun. Math. Sci.* 15 (2017) 1107–1128.

- [21] Y.Y. Cai, Y. Wang, A uniformly accurate (UA) multiscale time integrator pseudospectral method for the nonlinear Dirac equation in the nonrelativistic limit regime, *ESAIM: Math. Model. Numer. Anal.* 52 (2018) 543–566.
- [22] P. Krämer, K. Schratz, X. Zhao, Splitting methods for nonlinear Dirac equations with Thirring type interaction in the nonrelativistic limit regime, preprint (<https://publikationen.bibliothek.kit.edu/1000087636>).
- [23] G. Lenz, B.J. Eggleton, N.M. Litchinitser, Pulse compression using fiber gratings as highly dispersive nonlinear elements, *J. Opt. Soc. Am. B* 15 (1998) 715–721.
- [24] W.C.K. Mak, B.A. Malomed, P.L. Chu, Slowdown and splitting of gap solitons in apodized Bragg gratings, *J. Mod. Opt.* 51 (2004) 2141–2158.
- [25] T. Ahmed, J. Atai, Bragg solitons in systems with separated nonuniform Bragg grating and nonlinearity, *Phys. Rev. E* 96 (2017) 032222.
- [26] S.A.M.S. Chowdhury, J. Atai, Moving Bragg grating solitons in a semilinear dual-core system with dispersive reflectivity, *Sci. Rep.* 7 (2017) 4021.
- [27] W. Bao, X.-G. Li, An efficient and stable numerical method for the Maxwell–Dirac system, *J. Comput. Phys.* 199 (2004) 663–687.
- [28] W. Bao, Y.Y. Cai, X.W. Xia, Q. Tang, Numerical methods and comparison for the Dirac equation in the nonrelativistic limit regime, *J. Sci. Comput.* 71 (2017) 1094–1134.
- [29] S. Shao, N.R. Quintero, F.G. Mertens, F. Cooper, A. Khare, A. Saxena, Stability of solitary waves in the nonlinear Dirac equation with arbitrary nonlinearity, *Phys. Rev. E* 90 (2014) 032915.
- [30] J. Cuevas-Maraver, P.G. Kevrekidis, A. Saxena, F. Cooper, F.G. Mertens, Solitary waves in the nonlinear Dirac equation at the continuum limit: Stability and dynamics, In: *Ord. Part. Diff. Eqs.*, (Nova Science, Boca Raton), Chap. 4.
- [31] G. Berkolaiko, A. Comech, On spectral stability of solitary waves of nonlinear Dirac equation in 1D, *Math. Model. Nat. Phenom.* 7 (2012) 13–31.
- [32] T.I. Lakoba, Numerical study of solitary wave stability in cubic nonlinear Dirac equations in 1D, *Phys. Lett. A* 382 (2018) 300–308.
- [33] S.Y. Lee, T.K. Kuo, A. Gavrielides, Exact localized solutions of two-dimensional field theories of massive fermions with Fermi interactions, *Phys. Rev. D* 12 (1975) 2249–2253.
- [34] A. Alvarez, B. Carreras, Interaction dynamics for the solitary waves of a nonlinear Dirac model, *Phys. Lett. A* 86 (1981) 327–332.
- [35] G.W. Stewart, *Introduction to Matrix Computations*, (Academic, New York, 1973); Secs. 6.2 and 6.6.

- [36] S.J. Orfanidis, R. Wang, Soliton solutions of the Massive Thirring model, *Phys. Lett. B* 57 (1975) 281–283.
- [37] S.-J. Chang, S.D. Ellis, B.W. Lee, Chiral confinement: An exact solution of the massive Thirring model, *Phys. Rev. D* 12 (1975) 3572–3582.
- [38] D.J. Kaup, A.C. Newell, On the Coleman correspondence and the solution of the Massive Thirring model, *Lett. Nuovo Cimento* 20 (1977) 325–331.
- [39] E.A. Kuznetsov, A.V. Mikhailov, On the complete integrability of the two-dimensional classical Thirring model, *Theor. Math. Phys.* 30 (1977) 193–200.
- [40] D.J. Kaup, T.I. Lakoba, The squared eigenfunctions of the massive Thirring model in laboratory coordinates, *J. Math. Phys.* 37 (1996) 308–323.
- [41] H.G. Winful, Pulse compression in optical fiber filters, *Appl. Phys. Lett.* 46 (1985) 527–529.
- [42] I.V. Barashenkov, D.E. Pelinovsky, E.V. Zemlyanaya, Vibrations and Oscillatory Instabilities of Gap Solitons, *Phys. Rev. Lett.* 80 (1998) 5117–5120.
- [43] S.M. Cox, P.C. Matthews, Exponential time differencing for stiff systems, *J. Comput. Phys.* 176 (2002) 430–455.
- [44] F. de la Hoz, F. Vardillo, An integrating factor for nonlinear Dirac equations, *Comput. Phys. Commun.* 181 (2010) 1195–1203.
- [45] X. Antoine, E. Lorin, A simple pseudospectral method for the computation of the time-dependent Dirac equation with Perfectly Matched Layers, *J. Comput. Phys.* 395 (2019) 583–601.
- [46] A. Khare, F. Cooper, A. Saxena, Approximate analytic solutions to coupled nonlinear Dirac equations, *Phys. Lett. A* 381 (2017) 1081–1086.
- [47] N.V. Alexeeva, I.V. Barashenkov, A. Saxena, Spinor solitons and their PT-symmetric offspring, *Ann. Phys.* 403 (2019) 198–223.
- [48] V.E. Zakharov, Collapse of Langmuir waves, *Sov. Phys. JETP* 35 (1972) 908–914.
- [49] T.I. Lakoba, Instability of the finite-difference split-step method applied to the nonlinear Schrödinger equation. II. moving soliton, *Numer. Methods Partial Differ. Equ.* 32 (2016) 1024–1040.